UC Santa Barbara

UC Santa Barbara Electronic Theses and Dissertations

Title

Computational Design and Morphology Engineering of Multiblock Polymer Films

Permalink

https://escholarship.org/uc/item/1g85s9dt

Author

Paradiso, Sean Phillip

Publication Date

2015

Peer reviewed|Thesis/dissertation

eScholarship.org Powered by the California Digital Library
University of California

UNIVERSITY OF CALIFORNIA
Santa Barbara

Computational Design and Morphology Engineering of Multiblock Polymer Films

A Dissertation submitted in partial satisfaction
of the requirements for the degree of

Doctor of Philosophy

in

Chemical Engineering

by

Sean Phillip Paradiso

Committee in Charge:

Professor Glenn H. Fredrickson, Chair

Professor Carlos García-Cervera

Professor Todd M. Squires

Professor M. Scott Shell

December 2015

The Dissertation of
Sean Phillip Paradiso is approved:

Professor Carlos García-Cervera

Professor Todd M. Squires

Professor M. Scott Shell

Professor Glenn H. Fredrickson, Committee Chair

October 2015

Computational Design and Morphology Engineering of Multiblock Polymer Films

Copyright © 2015

by

Sean Phillip Paradiso

To my parents and grandfather

Acknowledgements

First and foremost I'd like to thank my adviser, Glenn Fredrickson, for his patience and guidance over the course of this thesis. My perspective on research and the kind of work that inspires me has changed significantly over the last five years, and I struggle to express how much I appreciate the grace with which Glenn accepted and accommodated this evolution. I would also like to thank the other members of my committee for their time and critical attention. In particular, Carlos Garcìa-Cervera and Hector Ceniceros were both integral to the development of the methods that enabled the first three chapters of this thesis.

One of the great joys of being involved in a research group is the opportunity to be mentored by and, eventually, mentor exceptional people. For taking the time to field underconsidered questions - research-related or not - on my slow meandering to competence, I am deeply thankful to Kris Delaney, Su-mi Hur, Mike Villet, Debbie Audus, Nabil Laachi, Wei Li, and Zoltan Mester. I'm also grateful to the rest of the "ensemble:" Carol Tsai, Jimmy Liu, Corinne Carpenter, Jonathan Martin, Doug Tree, Jeff Gopez, and Ed Toumayan for making these past few years so rich and enjoyable. I especially thank Mike Carilli, my imitable office-mate, for his willingness to "just take a look at something" for what he knows will be hours, thoughtful conversation, and cathartic commiseration.

I'd also like to take a moment to appreciate all of the local climbers I've had the great pleasure of falling off rocks with over the years. Notably Greg Su, Arthur Guittet, Darice Lee, Kerim Tshimanga, Li Zhiqun, Ben Caillat, Alex Spott, Peter Mage, Matt Gebbie, Antonio Labaro, Robb Messinger, and Mike Villet, but many, many others. Thank you for helping me see how truly beautiful the world is in all its colors and textures. Every trip was an adventure I won't soon forget.

Finally, I thank Stephanie for her love and patience, my grandparents for their unique and invaluable perspectives, and my parents for their unwavering support in the face of many a self-set fire.

Curriculum Vitæ

Sean Phillip Paradiso

Education

2015	Doctor of Philosophy in Chemical Engineering, University of California, Santa Barbara.
2010	Bachelor of Science in Chemical Engineering, University of Massachusetts, Amherst.

Awards and Fellowships

2014	CSP Technologies Fellowship
2014	Best Oral Presentation Clorox-Amgen Graduate Student Symposium
2012	Scienceline Outstanding Answerer Award
2010	Heslin Fellowship
2010	Million Heirs Fellowship

Publications

S.P. Paradiso, K.T. Delaney, G.H. Fredrickson, "A Swarm Intelligence Platform for Multiblock Polymer Inverse Design," In preparation.

S.P. Paradiso, K.T. Delaney, C. Garcìa-Cervera, G.H. Fredrickson, "Cyclic Solvent Annealing Improves Feature Orientation in Block Copolymer Thin Films," In preparation.

S.P. Paradiso, K.T. Delaney, C. Garcìa-Cervera, G.H. Fredrickson, "Block Copolymer Self Assembly During Rapid Solvent Evaporation: Insights Into Cylinder Growth and Stability," *ACS Macro Letters*.

Selected Presentations

2014	APS March Meeting, San Antonio, TX
2014	UCSB Graduate Student Symposium, Santa Barbara, CA
2013	Mini Stat Mech Meeting, Berkeley, CA
2013	APS March Meeting, Baltimore, MD
2012	APS March Meeting, Boston, MA

Abstract

Computational Design and Morphology Engineering of Multiblock Polymer Films

Sean Phillip Paradiso

In recent years, block copolymers have grown in popularity as a platform for building functional, nanostructured materials. The innate ability of inhomogeneous block copolymers to self assemble into a broad array of highly ordered mesostructures has generated interest for applications in advanced membranes, electronic materials, and nanostructured resist masks for lithography, among others. As the design requirements of these applications mature and more ambitious projects are imagined, the ability to intuitively design complex formulations of multiblock polymers will quickly saturate. Here, we study multiblock polymer self assembly to better understand, and therefore enhance our ability to engineer, the process to producing nanostructured polymer materials.

The primary drive of our investigation is to understand pattern selection during solvent evaporation, a method for producing block copolymer materials that is gaining popularity due to the control it offers over the self assembly process. To this end, we describe a field-based dynamics method for simulating the microphase separation process during solvent evaporation and offer insights into the physical parameters that appear to govern the process.

In the final chapter, we zoom out and approach the general problem of multiblock polymer design as a global optimization problem. The combinatoric explosion of choices for multiblock polymer architectures (arrangement, chemistry, connectivity) and blends threatens to curtail future development if robust automation procedures are not identified to aid in the molecular discovery process. We describe a swarm intelligence platform here that offers an efficient and highly flexible interface to screening on any computable equilibrium property of interest, using morphology as a motivating example.

Contents

List of Figures

Chapter 1

Introduction

One of the key challenges in polymer materials production is the complex rheology and slow internal relaxation times that polymeric materials exhibit during, and potentially after, processing. These factors often contribute to materials being formed far from equilibrium and requiring further annealing in order to perform reliably or exhibit optimal properties. In simple blends, this annealing process may facilitate a number of processes, such as ensuring even dispersion of blend components or the relaxation of residual mechanical stress established in the material during processing. For block copolymers, however, the need for annealing is more urgently motivated by the fact that equilibrium self assembly processes are often principally responsible for lending the material its desirable properties. For instance, advanced membranes utilizing block copolymers that self assemble

into nanoscopic cylinders have the potential to serve as efficient size-exclusion filters for industrial separations[1–3]. The performance of these membranes relies critically on the self assembled cylinders forming in an orientation that runs along the separation axis, as well as achieving a well-ordered state free of pore-closing defects. Without a reliable annealing procedure that grants sufficient control over the self assembly process to ensure that all of these morphology quality targets are met, block copolymers as a material platform look much less attractive.

The current standard for annealing is a straightforward thermal process, where the material is heated until the constituent chains gain sufficient mobility to equilibrate. For applications where a great deal of control over the process of self assembly is required, however, solvent processing offers many advantages. First, the selection of various solvents can be used to tune effective interactions between copolymer blocks leading to a mitigation of surface preferentiality or, in extreme cases, changing the equilibrium morphology entirely[4]. During evaporation, the loss of solvent will lead to structural rearrangements through a dynamical process that involves multiple timescales of solvent interdiffusion, surface transport, and chain relaxations over molecular and mesoscopic length scales. Of course, any means of distinguishing between states can be the basis for engineering a process to favor one over the other. It is one of the primary goals of this thesis to track the

morphology development during solvent treatment in order to understand how to realize this degree of control.

Understanding the ordering process during solvent annealing is the primary focus of the first three chapters of this thesis. In chapter 2, we formulate a dynamical field theory from a coarse-grained particle model of a block copolymer and solvent system. We further describe a semi-implicit numerical strategy for solving the resulting dynamics equations and address a number of issues associated with incorporating solvent evaporation into the field theory framework and solving the equations on a dynamic domain.

In chapter 3, we focus on the evaporation-induced self assembly problem and bring a small amount of clarity to questions raised over a decade of experimental evidence regarding the extent to which rapid solvent evaporation drives the oriented growth of block copolymer microphases. One of the key conclusions from this study is the establishment of a direct link between the architecture of the block copolymers and the stability of the ordering front generated during evaporation. Another, rather unfortunate, conclusion of this work is that the window for stability for generating stable ordering fronts is quite small, consistent with the wide variability in experimental success with the method[5–7].

The evidence that evaporation-induced self assembly has a fundamentally limited ability to reliably generate well aligned features motivated us to consider al-

ternative solvent processing techniques. One of the primary drawbacks of leveraging evaporation-induced ordering to drive feature orientation in block copolymer films is that there is no clear path towards systematically improving the order in the film after it is cast. In an attempt to address this shortcoming, we adapt the evaporation dynamics to reversibly take on and remove solvent through a cyclic annealing process. This strategy attempts to exploit the fact that the lamellar and cylindrical microphases both respond very differently to applied stress along their axial and lateral dimensions. In chapter 4, we explore the degree to which this anisotropic stress response can be used as a selection mechanism for encouraging the formation of highly ordered and vertically oriented lamellae and cylinders. Both static solvent annealing and cyclic thermal annealing were simulated to generate a baseline for comparison with the cyclic solvent annealing method. In aggregate, the results are strongly suggestive that cyclic swelling and deswelling of films may be an excellent way to generate highly ordered and, importantly, oriented structures in thin block copolymer films.

Finally, in addition to the work on solvent processing, we take a broader look at the problem of molecular discovery for block polymer materials. The block copolymer community is at a defining moment where the ability to synthetically prepare exotic block polymer architectures has outstripped our ability to systematically propose promising architectures based on a set of desired properties. The

community finds itself in a somewhat awkward place as a consequence. On the one hand, the degree of fine-tuned control over nanoscale morphology afforded by a block polymer of arbitrary architectural complexity is likely to revolutionalize our ability to architect new nanomaterials. On the other hand, the link between equilibrium morphology and chain architecture appears to be too complex to design molecules intuitively with a certain nanostructure in mind, and the combinatoric explosion of options when choosing a molecular design renders an exhaustive search entirely prohibitive[8]. In chapter 5, we report a method that attempts to address this problem by providing a means to automate the efficient search through block polymer design parameters (number of blocks, length of each block, connectivity, and blend ratio with other block copolymers) based on computable properties of the resulting blend using standard field theory tools. We use the following problem of morphology selection as a motivating example: given a desired pattern (monomer distribution), identify a block copolymer or blend of block copolymers that would self assemble into a matching pattern at equilibrium. Our approach is not peculiar to morphology optimization, however, and should generalize quite easily to optimize on any computable equilibrium property.

Chapter 2

Field theory model of block copolymers

The problem of evaporation-induced self assembly (EISA) is compelling both for its practical importance to the solution-casting process for building nanostructured materials from block copolymers[4, 9–11] as well as the opportunity to kinetically trap nonequilibrium morphologies[12]. In order to study this phenomena in detail, however, a computational strategy must be developed that is able to accommodate the multiple length and time scales in the problem. The critical need for flexibility in selecting the coarse-grained physics of this complex process compells us to seek a field theoretic description of self assembly.

In this chapter, we motivate and derive a dynamical field theory capable of efficiently simulating the long wavelength concentration dynamics of microphase separation during solvent evaporation. We'll reuse an extension of this framework in chapter 5 where we leverage some of the advantages of the field-based description to perform inverse design calculations.

2.1 Block copolymer solution model

We begin from a particle-based model of a diblock copolymer solution in order to emphasize the approximations underlying the dynamical field theory that is the ultimate result of this section.

2.1.1 Particle-based model

Our approach to building a model of collective variable dynamics will rest on a near-equilibrium assumption, so we start by describing the solvated diblock copolymer system at equilibrium. Our system is comprised of n_p copolymer chains of length N and block fraction f_A with n_s solvent particles, illustrated schematically in Figure 2.1. For simplicity, we assume that each solvent particle occupies the same molecular volume as each of the N monomers comprising the polymer, denoted v_0. As we are expressly interested in phase behavior and concentration

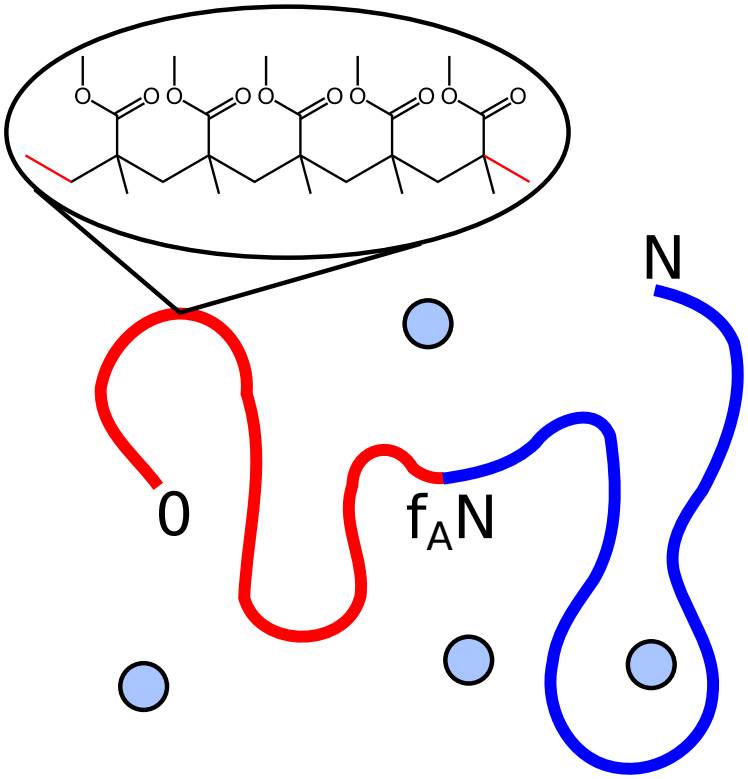

Figure 2.1: The ingredients of our block copolymer solution system. The coarse-grained polymer chains consist of continuous segments whose properties (equilibrium bond length, bending rigidity, etc.) represent an underlying chemical structure. Here, as an example, the A block is comprised of methyl-methacrylate monomers.

dynamics, the central object of interest for computing thermodynamic properties

will be the configurational part of the canonical partition function, $\mathcal{Z}_C$, which for

the block copolymer solution system may be written as:

$$\begin{aligned}\mathcal{Z}_C(n_s, n_p, V, T) = &\frac{1}{(n_p!)\,(n_s!)\,(\lambda_T^3)^{n_s+n_pN}} \prod_{j=1}^{n_p} \int \mathcal{D}\mathbf{R}_j(s) \prod_{k=1}^{n_s} \int d\mathbf{R}_k \\ &\times \exp\left(-\beta U_{el}[\mathbf{R}^{n_p}(s)] - \beta U_{int}[\mathbf{R}^{n_p}(s), \mathbf{R}^{n_s}]\right) \\ &\times \exp\left(-\beta U_{cmp}[\mathbf{R}^{n_p}(s), \mathbf{R}^{n_s}]\right)\end{aligned} \tag{2.1}$$

where the potential energy is comprised of three contributions: U_{el}, U_{int}, and U_{cmp}, $\beta = 1/k_BT$ is the Boltzmann factor, and the functional integral represents an enumeration of all polymer chain conformations represented by volume-filling space curves $\mathbf{R}^{n_p}(s)$ and solvent particle positions $\mathbf{R}^{n_s}$.

The first contribution to the potential energy accounts for the stretching energy associated with a polymer conformation. We use the simple continuous Gaussian chain model[13] for our calculations, which is accurate for weakly stretched chains, and for which the elastic energy of a system of n_p chains is:

$$\beta U_{el} = \frac{3}{2b^2} \sum_{j=1}^{n_p} \int_0^N ds \left| \frac{\partial \mathbf{R}_j(s)}{\partial s} \right|^2 \tag{2.2}$$

where b is, by construction, the equilibrium root-mean-square distance between two contour points separated by $\Delta s = 1.0$ along the chain for a chain following this stretching potential.

The second contribution accounts for inter-monomer interaction energies, for which we use the following pair decomposition for the potential of mean force between segments:

$$U_{int} = \frac{1}{2}\sum_{j=1}^{n_p}\sum_{k=1}^{n_p}\int ds \int ds' u(|\mathbf{R}_j(s) - \mathbf{R}_k(s')|) \tag{2.3}$$

In this thesis, we are concerned with mesoscale phenomena related to microphase separation that occurs over length scales more comparable to full chains than single monomers. For this reason, it is appropriate (and highly attractive looking forward to numerical strategies) to replace the pair potential with a delta function interaction scaled by the Flory-Huggins parameter - a model that has been used to faithfully predict copolymer phase behavior[13, 14]:

$$\beta U_{int} = \frac{v_0}{2}\sum_{J=A,B,S}\sum_{K=A,B,S}\int d\mathbf{r}\chi_{JK}\widehat{\rho}_J(\mathbf{r})\widehat{\rho}_K(\mathbf{r}) \tag{2.4}$$

where we have introduced local monomer/particle segment density operators

$$\begin{aligned}\widehat{\rho}_A(\mathbf{r}) &= \sum_{j=1}^{n_p}\int_0^{f_A N} ds\ \delta\left(\mathbf{r} - \mathbf{R}_j(s)\right)\\ \widehat{\rho}_B(\mathbf{r}) &= \sum_{j=1}^{n_p}\int_{f_A N}^{N} ds\ \delta\left(\mathbf{r} - \mathbf{R}_j(s)\right)\end{aligned} \tag{2.5}$$

for polymer species, where f_A is the fraction of A monomers in the diblock chains, and

$$\widehat{\rho}_S(\mathbf{r}) = \sum_{j=1}^{n_s} \delta\left(\mathbf{r} - \mathbf{R}_j\right) \tag{2.6}$$

for the solvent component.

Finally, it will be convenient later to admit a small but finite compressibility at the level of the thermodynamic model. For small deviations from a uniform density, the energy penalty can be approximated by a harmonic potential scaled by a compressibility factor:

$$\beta U_{cmp} = \frac{v_0 \zeta}{2} \int d\mathbf{r} \left(\sum_J \widehat{\rho}_J(\mathbf{r}) - \rho_0 \right)^2 \tag{2.7}$$

where ζ is the compressibility factor and $\rho_0 = 1/v_0$ is the volume averaged monomer density. Combining these together, we arrive at the particle based partition function for the solvated A-*b*-B diblock system.

2.1.2 Field-based model

The final result from the previous section has made a modest but important step towards a coarse-grained theory that can be used to sudy the mesoscale behavior of a copolymer solution, namely the recasting of inter-monomer interactions in terms of microscopic density operators. The next step is to completely decou-

ple interactions between individual chains by means of a Hubbard-Stratonovich transformation. By introducing a functional analogue to the complex exponential representation of the delta function into (2.1):

$$\delta[\rho(\mathbf{r}) - \widehat{\rho}(\mathbf{r})] = \int \mathcal{D}w \exp\left(-i \int d\mathbf{r} w(\mathbf{r}) \left(\rho(\mathbf{r}) - \widehat{\rho}(\mathbf{r})\right)\right) \tag{2.8}$$

and using the identity $\int \mathcal{D}\rho\delta(\rho - \widehat{\rho})F[\widehat{\rho}] = F[\rho]$, we can rewrite the partition function in the following form:

$$\frac{\mathcal{Z}_C}{\mathcal{Z}_0} = \int \mathcal{D}\rho_A \int \mathcal{D}\rho_B \int \mathcal{D}\rho_S \int \mathcal{D}w_A \int \mathcal{D}w_B \int \mathcal{D}w_S \exp\left(-\beta H\right) \tag{2.9}$$

where

$$\begin{aligned}\beta H = \frac{v_0}{2} \sum_{i,j} \int d\mathbf{r} \rho_i(\mathbf{r}) \rho_j(\mathbf{r}) \chi_{ij} - \sum_j \int d\mathbf{r} i w_j(\mathbf{r}) \rho_j(\mathbf{r}) + \frac{v_0 \zeta}{2} \int d\mathbf{r} \left(\sum_i \rho_i(\mathbf{r}) - \rho_0\right)^2 \\ - n_p \log Q_{AB}[w_A, w_B] - n_s \log Q_S[w_S]\end{aligned} \tag{2.10}$$

The analytical work done by the transformation has taken an integral over interacting chain degrees of freedom and cleanly separated it into three terms: a functional integral over interacting density fields, a similar term including a complex auxiliary potential introduced in the delta functionals above, and a pair of

single-molecule partition functions Q_{AB} and Q_S. All remaining chain/particle position degrees of freedom are enumerated in the Q terms, which may be computed as

$$\begin{aligned} Q_{AB}[w_A, w_B] &= \frac{1}{V}\int d\mathbf{r} q(\mathbf{r}, N; w_A, w_B) \\ Q_S[w_S] &= \frac{1}{V}\int d\mathbf{r} \exp\left(-i w_s(\mathbf{r})\right) \end{aligned} \tag{2.11}$$

These are the partition functions that normalize the probability distribution over space of monomers and solvent particles experiencing an applied external potential. This enumeration of states can be performed directly in the case of the solvent component, but the partition function for a single polymer chain is computed with the aid of a propagator that satisfies the following Fokker-Planck equation:

$$\partial_s q(\mathbf{r}, s) = \nabla^2 q(\mathbf{r}, s) - w(\mathbf{r}) q(\mathbf{r}, s) \tag{2.12}$$

representing the statistical weight of a segment at position s along a chain being found at point $\mathbf{r}$ in space with the intuitive initial condition that $q(\mathbf{r}, s = 0) = 1$ as a chain of no length experiences no field.

2.1.3 Concentration dynamics

The concentration dynamics used in our calculations are based on the dynamical Self Consistent Field Theory (DSCFT) method[15, 16], that we extend here to model block-copolymer self assembly in the presence of volatile solvents [17]. In this framework, the field theory description of a linear A-*b*-B diblock copolymer in explicit solvent derived in the previous sections is used to compute the chemical potential fields $\mu_i(\mathbf{r}, t)$ that drive collective motion according to the following diffusive dynamics:

$$\begin{aligned} \partial_t \rho_i(\mathbf{r}, t) &= -\nabla \cdot \mathbf{J}(\mathbf{r}, t) \\ &= \nabla \cdot \sum_j \int d\mathbf{r}' \Lambda_{ij}(\mathbf{r} - \mathbf{r}') \nabla \mu_j(\mathbf{r}', t) \\ &\quad + \eta_i(\mathbf{r}, t) \end{aligned} \tag{2.13}$$

where i indexes the monomer species, ρ_i is the concentration of monomer/solvent species i, Λ_{ij} is an Onsager coefficient matrix, and η_i is a Gaussian noise source, whose inclusion is necessary to sample trajectories that feature thermally activated defect annihilation events. Multiple expressions have been derived under different kinetic approximations for the mobility kernel, Λ_{ij}, from the local coupling[16] model used here to more accurate non-local kernels based on the

Rouse and reptation models[16, 18]. The appropriate choice for Λ_{ij} in the local coupling approximation may be derived in the manner of de Gennes[19].

The derivation is based on the Flory-Huggins free energy, however we stress that the full field theory is fully compatible with the Flory-Huggins model over large length scales. Our primary concern is to identify the proper kinetic scaling for the solvent and polymer components, so, as in the reference above, we treat the copolymer as a homopolymer of length N:

$$\begin{aligned} \beta F = \frac{v_0}{2} \int d\mathbf{r} \sum_{ij} \rho_i(\mathbf{r}) \rho_j(\mathbf{r}) \chi_{ij} \\ + \frac{1}{N} \rho_P \log \rho_P + \rho_S \log \rho_S \end{aligned} \tag{2.14}$$

Computing the chemical potential field $\mu = \delta \beta F / \delta \rho$ from (2.14), neglecting the χ term, and inserting the result into (2.13) yields:

$$\begin{aligned} \partial_t \rho_p &= \nabla \cdot \int d\mathbf{r}' \Lambda_{pp}(\mathbf{r} - \mathbf{r}') \frac{1}{N} \frac{1}{\rho_p(\mathbf{r})} \nabla \rho_p(\mathbf{r}) \\ \partial_t \rho_s &= \nabla \cdot \int d\mathbf{r}' \Lambda_{ss}(\mathbf{r} - \mathbf{r}') \frac{1}{\rho_s(\mathbf{r})} \nabla \rho_s(\mathbf{r}) \end{aligned} \tag{2.15}$$

To determine the appropriate form and scalings for the Onsager kernels, we define an intrinsic diffusivity as $\partial_t \rho_i = \nabla \cdot \tilde{D} \nabla \rho_i$. Asserting a polymer segment diffusivity proportional to $\tilde{D} = D_0 N_e / N^2$, where N_e is the number of segments between entanglements, and solvent diffusivity $\tilde{D} = D_0$, we find $\Lambda_{ij} = D_0 \delta_{ij} (N_e / N) \rho_j \delta(\mathbf{r} -$

$\mathbf{r}'$) for the monomer fields and $\Lambda_{ij} = D_0\delta_{ij}\rho_j\delta(\mathbf{r}-\mathbf{r}')$ for solvent. Here, we model unentangled polymer chains for which $N_e/N = 1$. With this in place, the dynamical equations simplify to:

$$\partial_t\rho_i(\mathbf{r},t) = \nabla\cdot\left(\frac{D_0}{N_i}\rho_i(\mathbf{r},\mathbf{t})\nabla\frac{\delta\beta H}{\delta\rho_i}\right) + \eta_i(\mathbf{r},t) \tag{2.16}$$

where $N_S = 1$, $N_{A,B} = N$ are molecular size parameters and the noise source is produced from a Gaussian distribution with moments $\langle\eta(\mathbf{r},t)\rangle = 0$, $\langle\eta_i(\mathbf{r},t)\eta_j(\mathbf{r}',t')\rangle = -2\nabla\cdot\frac{D_0}{N_j}\rho_j(\mathbf{r},t)\nabla\delta(\mathbf{r}-\mathbf{r}')\delta_{ij}\delta(t-t')$. Finally, we join the derived kinetic coefficients above with more accurate chemical potential fields $\delta\beta H/\delta\rho_i$ computed from the full SCFT free-energy[15, 20]:

$$\begin{aligned}\beta H = &\sum_{ij}\int\frac{1}{2\rho_0}\chi_{ij}\rho_i(\mathbf{r})\rho_j(\mathbf{r})d\mathbf{r}\\ &-\sum_i\int w_i(\mathbf{r})\rho_i(\mathbf{r})d\mathbf{r}\\ &+\int\frac{\zeta}{2\rho_0}\left(\sum_i\rho_i(\mathbf{r})-\rho_0\right)^2 d\mathbf{r}\\ &-n_S\log\left(Q_S[w_S(\mathbf{r})]\right) - n_{BCP}\log\left(Q_{AB}[w_A(\mathbf{r}),w_B(\mathbf{r})]\right),\end{aligned} \tag{2.17}$$

where $\beta = 1/k_BT$ is the well known Boltzmann factor, χ_{ij} is a matrix of Flory-Huggins interaction parameters, ρ_0 is the average particle density (the particle

volume $v_0 = \frac{1}{\rho_0}$ is taken to be the same for monomer and solvent particles), n_S is the total number of solvent particles, n_{BCP} is the total number of copolymer chains, and ζ is a Helfand compressibility penalty. The thermodynamic forces in (2.16) may then be computed as:

$$\frac{\delta\beta H}{\delta\rho_i} = \frac{1}{\rho_0}\left(\sum_j \chi_{ij}\rho_j\right) - w_i^*(\mathbf{r}) + \frac{\zeta}{\rho_0}\left(\sum_i \rho_i(\mathbf{r}) - \rho_0\right), \tag{2.18}$$

with the self-consistent field $w_i^*(\mathbf{r})$ chosen for species i=A or B at each time step to satisfy the partial saddle point condition:

$$\left.\frac{\delta\beta H}{\delta w_i}\right|_{w_i^*} = 0 = -\frac{n_{BCP}}{Q_{AB}}\frac{\delta Q_{AB}}{\delta w_i(\mathbf{r})} - \rho_i(\mathbf{r},t), \tag{2.19}$$

The first terms in (2.19) may be written in terms of the forward and reverse propagators (q, $q^\dagger$) for a single diblock copolymer chain in an external field:

$$\begin{aligned}
\frac{-n_{BCP}}{Q_{AB}}\frac{\delta Q_{AB}}{\delta w_A(\mathbf{r})} &= \frac{n_{BCP}}{VQ_{AB}}\int_0^{f_A N} q(\mathbf{r},s)q^\dagger(\mathbf{r},N-s)ds, \\
\frac{-n_{BCP}}{Q_{AB}}\frac{\delta Q_{AB}}{\delta w_B(\mathbf{r})} &= \frac{n_{BCP}}{VQ_{AB}}\int_{f_A N}^{N} q(\mathbf{r},s)q^\dagger(\mathbf{r},N-s)ds,
\end{aligned} \tag{2.20}$$

where $q(\mathbf{r},s)$ represents the statistical weight of a segment at position s along the polymer backbone being found at point $\mathbf{r}$ in space and satisfies the following

Fokker-Planck equation:

$$\begin{aligned} \partial_s q(\mathbf{r}, s) &= \frac{b^2}{6}\nabla^2 q(\mathbf{r}, s) - w(\mathbf{r}, s) q(\mathbf{r}, s), \\ q(\mathbf{r}, 0) &= 1. \end{aligned} \tag{2.21}$$

where $w(\mathbf{r}, s) = w_A(\mathbf{r})\theta\left(f_A N - s\right) + w_B(\mathbf{r})\theta\left(s - f_A N\right)$ and $\theta(s)$ is the Heaviside function. The reverse propagator $q^\dagger$ satisfies the same equation, but with the field identities (w_A, w_B) reversed so that $w^\dagger(\mathbf{r}, s) = w_B(\mathbf{r})\theta\left((1 - f_A)N - s\right) + w_A(\mathbf{r})\theta\left(s - (1 - f_A)N\right)$. For the solvent species S, the self-consistent field may be computed directly as:

$$w_S^*(\mathbf{r}) = -\log\left(\frac{\rho_S(\mathbf{r}, t)}{n_S/V}\right). \tag{2.22}$$

Although the SCFT equations relevant to this discussion have been detailed in previous sections and elsewhere in the literature[20, 21], we have sketched out the hierarchy here to highlight the presence of two sets of boundary conditions that must be specified: one for the dynamical density fields $\rho_i(\mathbf{r}, t)$ and one for the copolymer propagators $q(\mathbf{r}, s)$ and $q^\dagger(\mathbf{r}, s)$. Importantly, these two sets of equations are coupled through (2.19), placing a compatibility constraint on the boundary conditions that may be imposed on each. For the substrate and lateral boundaries, homogeneous Neumann and periodic boundary conditions, respec-

tively, may be applied to each set of equations with no conflict. The free surface, however, must feature a non-zero solvent flux which, due to near incompressibility, requires an approximately equal and opposite flux of polymer at the free surface boundary (a physical condition resulting from the changing domain due to lost mass as discussed in the proceeding section). This presents a problem in the solution of (2.21), for while the gradient of the density operator at the free surface may be computed as an integral involving the gradient of the propagator, the inverse relationship is not available without resorting to iteration. Computing this inverse at each time step to ensure the appropriate non-zero Neumann-type boundary conditions would be prohibitively expensive. In order to bring the boundary conditions on the dynamics equations in accord with the propagators in equations (2.20) and (2.21), we instead have chosen to redistribute the flux from a boundary condition on the solvent field to a source term in the dynamics:

$$\begin{aligned}\partial_t \rho_S(\mathbf{r},t) =& \nabla \cdot \left(D_0 \rho_S(\mathbf{r},t) \nabla \frac{\delta \beta H}{\delta \rho_S} \right) \\ &+ \eta_S(\mathbf{r},t) + 2R(\mathbf{r},t)\delta(z - L_z(t)),\end{aligned} \tag{2.23}$$

where the Dirac delta function serves to localize the mass loss at the time-dependent free surface position $L_z(t)$ and the factor of two accounts for the delta function having been centered on the boundary. With this transformation in place, homogeneous Neumann boundary conditions may then be applied at the

free surface to both the dynamical density fields and polymer propagators without conflict. The following section will derive an appropriate expression for the solvent source strength $R(\mathbf{r}, t)$.

2.1.4 Modeling evaporation

In order to model the uptake of solvent in the field-theory framework, we employ a simple linear mass transfer model for the flux at the film/vapor boundary. In a typical solvent annealing chamber, thin films are exposed to an atmosphere of fixed solvent partial pressure P_S. At equilibrium, the concentration of solvent in the film is given by the following VLE equation (for low pressures, we neglect the Poynting correction and treat the vapor phase as an ideal gas):

$$a\phi_S P_S^{sat}(T, P) = P_S, \tag{2.24}$$

where a is the solvent activity, $\phi_S = \rho_S/\rho_0$ is the volume fraction of solvent in the film, and P_S^{sat} is the saturated vapor pressure of solvent at the annealing conditions. To first order, we can approximate the solvent flux as proportional to the difference between these two factors which, after treating each volume element

at the surface as an independent Hertz-Knudsen system[22], becomes:

$$J_S(\mathbf{r},t) = k\rho_0 a P_S^{sat}\left(\phi_S(\mathbf{r},t) - \phi_S^{eq}\right), \tag{2.25}$$

where k is a mass transfer coefficient and we have defined an equilibrium surface solvent concentration $\phi_S^{eq} = \frac{P_S}{aP_S^{sat}}$. It is understood that this expression is only valid at the free surface. We can now revisit the source term introduced in the previous section. Since integrating (2.23) over the domain should result in equivalent solvent loss as the expression for the flux above, we set $R(\mathbf{r},t) = -J_S(\mathbf{r},t) = -k\rho_0 a P_S^{sat}\left(\phi_S(\mathbf{r},t) - \phi_S^{eq}\right)$.

Finally, as solvent enters or leaves the system, the domain will expand/contract to accommodate the added or lost volume. We neglect time variations in the lateral dimensions of the simulation cell and write an equation of motion for the film thickness as a function of time:

$$\frac{dV}{dt} = -v_0 \int_V J_S(\mathbf{r},t)\delta\left(\mathbf{r}\cdot\widehat{\mathbf{e}}_z - L_z(t)\right) d^3\mathbf{r} \tag{2.26}$$

which, after isolating the equation of motion for the film thickness and combining with (2.25) becomes:

$$\frac{dL'_z}{dt'} = -\frac{NB_i}{L'_x L'_y} \int_A (\phi_S(\mathbf{r}'_\perp, t) - \phi_S^{eq})\, d^2\mathbf{r}'_\perp, \tag{2.27}$$

where we've introduced the dimensionless quantities $L' = L/R_g$, $t' = t\frac{D_0}{NR_g^2}$, and a dimensionless "Biot number" $B_i = \frac{kaP_S^{sat}R_g}{D_0}$, and it is understood that the $\mathbf{r}'_\perp$ integral is taken over the free surface. Taken together, these equations provide a direct mapping from experimentally accessible parameters to the variables in our model that control solvent flux into and out of the simulated film. Note that in order to avoid solving the dynamics on a transient domain, we ultimately work in reduced units $z'(t) = \frac{z}{L'_z(t)}$ (a familiar transformation in Stefan problems[23, 24]).

2.1.5 Model summary

Here we briefly summarize the model equations and dimensionless quantities that characterize the cyclic annealing process:

$$\begin{aligned}
\partial_{t'}\phi_A &= \nabla_{\mathbf{r}'}\cdot(\phi_A\nabla_{\mathbf{r}'}N\mu_A) + \eta'_A,\\
\partial_{t'}\phi_B &= \nabla_{\mathbf{r}'}\cdot(\phi_B\nabla_{\mathbf{r}'}N\mu_B) + \eta'_B,\\
\partial_{t'}\phi_S &= \nabla_{\mathbf{r}'}\cdot(N\phi_S\nabla_{\mathbf{r}'}N\mu_S) + \eta'_S\\
&\quad - 2NB_i\left(\phi_S - \phi_S^{eq}\right)\delta_{\mathbf{r}'}(z - L_z(t)),
\end{aligned} \tag{2.28}$$

where $t' = t\frac{D_0}{NR_g^2}$, $B_i = \frac{kaP_S^{sat}NR_g}{D_0}$, $\mathbf{r}' = \frac{\mathbf{r}}{R_g}$, $\phi_i = \frac{\rho_i}{\rho_0}$, $\mu_i = \frac{\delta\beta H}{\delta\rho_i}$, and $\phi_S^{eq} = \frac{P_S}{aP_S^{sat}}$, and the Gaussian random fields are generated with the following moments[25, 26]:

$$\begin{aligned}
\langle\eta'_i(\mathbf{r}',t)\rangle &= 0\\
\langle\eta'_i(\mathbf{r}',t)\eta'_i(\mathbf{r}'',t')\rangle &= -\frac{2}{C}\nabla'_{\mathbf{r}}\cdot\phi_j\nabla'_{\mathbf{r}}\delta(\mathbf{r}'-\mathbf{r}'')\delta(t-t'),
\end{aligned} \tag{2.29}$$

where $C = \rho_0 R_g^3/N_i$ is the familiar dimensionless chain density which serves to control the fluctuation strength.

2.2 Solution techniques

2.2.1 Numerical methods

The set of coupled dynamical equations in (2.28) poses challenges for deriving an efficient and stable time stepping scheme due to the stiff gradient operators, variable mobility, and highly nonlinear chemical potential fields. In this section, we provide a brief derivation of the numerical methods implemented here, based on previous work with the Cahn-Hilliard equation[27].

For clarity, we omit the straightforward noise and surface flux terms that can be treated explicitly and start from a set of coupled, generalized diffusion equations of the form

$$\partial_t \phi_i(\mathbf{r}, t) = \nabla \cdot M_i(\mathbf{r}, t) \nabla \mu_i(\mathbf{r}, t). \tag{2.30}$$

The first step in the derivation is to extract the linear part of the chemical potential fields in the $\phi_i(\mathbf{r}, t)$ variable, $\mu_i^{lin}(\mathbf{r}, t)$. Adding and subtracting this term from the original field leads to

$$\partial_t \phi_i(\mathbf{r}, t) = \nabla \cdot M_i(\mathbf{r}, t) \nabla \left(\mu_i(\mathbf{r}, t) + \mu_i^{lin}(\mathbf{r}, t) - \mu_i^{lin}(\mathbf{r}, t) \right). \tag{2.31}$$

Inserting a forward difference approximation to the time derivative and evaluating the first linearized force term at the future time yields the following semi-implicit scheme:

$$\phi_i(\mathbf{r}, t+\Delta t) - \phi_i(\mathbf{r}, t) = \Delta t \nabla \cdot M_i(\mathbf{r}, t) \nabla \left(\mu_i(\mathbf{r}, t) + \mu_i^{lin}(\mathbf{r}, t+\Delta t) - \mu_i^{lin}(\mathbf{r}, t) \right). \tag{2.32}$$

Recall that, in the partial saddle-point approximation (2.19), the Hamiltonian is evaluated at $w_i(\mathbf{r}) = w_i^*(\mathbf{r}, t; \phi_i(\mathbf{r}, t))$, an implicit function of $\phi_i(\mathbf{r}, t)$. Ideally, one would consider the response of $w_i^*(\mathbf{r}, t)$ to perturbations around an arbitrary field configuration $\phi_i(\mathbf{r}, t)$ in order to accurately extrapolate the chemical potentials $\mu_i(w_i^*, \phi_i)$. However, the two-point response function to perturbations about a spatially inhomogeneous state proves far too expensive to compute in practice. Instead, we expand $w_i^*(\mathbf{r}, t)$ to first order in composition fluctuations about a *homogeneous state* $\left(\Delta\phi_i(\mathbf{r}, t) = \phi_i(\mathbf{r}, t) - \overline{\phi}_i(t)\right)$ where $\overline{\phi}_i(t)$ is the volume averaged i-type monomer concentration. Combining with (2.18), we obtain a computationally tractable expression for $\mu_i^{lin}(\mathbf{r}, t)$ as[20, 28]

$$\mu_i^{lin}(\mathbf{r}, t) = \sum_j \left(\chi_{ij} N + \zeta N\right) \phi_j(\mathbf{r}, t) - \int g_{ij}^{-1}(\mathbf{r} - \mathbf{r}') \Delta\phi_j(\mathbf{r}', t) d^3\mathbf{r}', \tag{2.33}$$

where $g_{ij}^{-1}(\mathbf{r}-\mathbf{r}',t)$ is the inverse of the familiar Debye scattering matrix obtained in the Random Phase Approximation[29] and the response kernel in the $w_i^*(\mathbf{r},t)$ expansion referenced above. At this point, we note that the difference $\left(\mu_i^{lin}(\mathbf{r},t+\Delta t)-\mu_i^{lin}(\mathbf{r},t)\right) \sim \mathcal{O}(\Delta t)$, so that in the limit $\Delta t \to 0$, error in the evaluation of the linearized terms will vanish, justifying any symmetric approximations made in the service of stability or computational convenience. As written, the variable mobility restricts our ability to write a semi-implicit update equation for $\phi_i(\mathbf{r},t+\Delta t)$. However, by replacing $M_i(\mathbf{r},t)$ with a constant factor (a) we may express the semi-implicit terms as simple products in Fourier space. With this replacement, and combining (2.32) with (2.33), we obtain

$$\begin{aligned}\phi_i(\mathbf{r},t+\Delta t) &= \phi_i(\mathbf{r},t)+\Delta t\nabla\cdot M_i(\mathbf{r},t)\nabla\mu_i(\mathbf{r},t)\\ &+\Delta t\ a\nabla^2\left(\sum_j\left(\chi_{ij}N+\zeta N\right)\phi_j(\mathbf{r},t+\Delta t)-\int g_{ij}^{-1}(\mathbf{r}-\mathbf{r}')\Delta\phi_j(\mathbf{r}',t+\Delta t)d^3\mathbf{r}'\right)\\ &-\Delta t\ a\nabla^2\left(\sum_j\left(\chi_{ij}N+\zeta N\right)\phi_j(\mathbf{r},t)-\int g_{ij}^{-1}(\mathbf{r}-\mathbf{r}')\Delta\phi_j(\mathbf{r}',t)d^3\mathbf{r}'\right).\end{aligned} \tag{2.34}$$

Taking the appropriate Fourier transforms of both sides of (2.34) consistent with the imposed boundary conditions (a plane wave basis along the lateral axes and cosine basis in the film thickness direction) and rearranging yields a conve-

nient update scheme for the resulting time-dependent amplitude equations:

$$\phi_i(\mathbf{k}, t + \Delta t) = \phi_i(\mathbf{k}, t) + \sum_j \Delta t A_{ij}^{-1}(\mathbf{k}) \mathcal{F}\left[\nabla \cdot M_j(\mathbf{r}, t) \nabla \mu_j(\mathbf{r}, t)\right], \tag{2.35}$$

where

$$A_{ij}(\mathbf{k}) = \left(1 + a\Delta t \left|\mathbf{k}\right|^2 \left(\chi_{ij} N + \zeta N - g_{ij}^{-1}(\mathbf{k})\right)\right). \tag{2.36}$$

As indicated above, the constant factor (a) may be chosen at will, although considering that large values favor stability at the expense of accuracy, a judicious choice should be made to balance the tradeoff. Here, we adopt the choice of Badalassi et al. [27] with $a = \max\left(M(\mathbf{r}, t)\right)/2$, which has been shown[30], in the context of the Cahn-Hilliard equations, to be the smallest value that yields unconditional stability for this first order, Euler-type discretization.

Finally, all neglected explicit terms can now be reintroduced inside the square brackets of the Fourier transform. These equations may be solved at each time step using a single forward/backward FFT (Fast Fourier Transform[31]) pair.

2.2.2 Ensuring conservation of mass

If one were to take the prescriptions above and integrate the equations of motion forward in time with the evaporation term turned on, they would be immediately confronted with rather confounding behavior: despite the equations being solved

with "no flux" boundary conditions, the total polymer density evidently decreases over time! The problem, perhaps obvious to the informed reader, is that homogeneous Neumann-type boundary conditions are only interpretable as "no flux" in the context of a static domain. In this section, we derive the rate of polymer loss and present two solutions we have implemented to ensure that the total number of polymer segments is preserved across an evaporation simulation. We note that this phenomenon has been identified previously by multiple authors and the first of our two solutions has the most literature precedent[23, 24].

We start from the conservation equation assuming only diffusive flux:

$$\partial_t \phi_i = \nabla \cdot M(\phi_i) \nabla \mu_i \tag{2.37}$$

In the physical systems of interest, typically a free-standing film will be thicker than the final dry film by a factor of 100-1000. During the drying process, the region of express interest is not the disordered wet polymer near the substrate but a narrow region near the free surface where microphase separation is initiated. For this reason, it is convenient, indeed essential, to apply a change of variables and solve the equations in a moving reference frame trained on this narrow window

near the free surface:

$$z' = \frac{z - L_0(t)}{L_1(t) - L_0(t)} = \frac{z - L_0(t)}{\Delta L} \tag{2.38}$$

where $L_0(t) = L_1(t) - \Delta L$ is the moving lower boundary, which follows the same equation of motion as (2.27). This change of variables adds a transport term to the equations of motion:

$$\partial_t \phi_i = \nabla \cdot M(\phi_i) \nabla \mu_i + \left(\frac{1}{\Delta L} \frac{dL_0(t)}{dt} \frac{\partial \phi}{\partial z'} \right)$$

Finally, recall that in order to remain consistent with the homogeneous Neumann conditions applied in the propagator equations (2.21), we use a localized sink term near the surface to evaporate solvent:

$$\partial_t \phi_i = \nabla \cdot M(\phi_i) \nabla \mu_i + \left(\frac{1}{\Delta L} \frac{dL_0(t)}{dt} \frac{\partial \phi_i}{\partial z'} \right) + g(z') B_i \left(\phi_i - \phi_i^{eq} \right)$$

where $g(z')$ is a normalized half-Gaussian centered on the free surface boundary:

$$g(z') = \frac{2}{\sqrt{2\pi\sigma^2}} e^{-\frac{(z'-1)^2}{2\sigma^2}}$$

Now, we apply the homogeneous Neumann boundary conditions on the flux:

$$M(\phi_i)\frac{\partial \mu_i}{\partial z'}\bigg|_{z'=0} = M(\phi_i)\frac{\partial \mu_i}{\partial z'}\bigg|_{z'=1} = 0$$

In order to compute the loss of polymer segments, we first integrate the monomer density over the domain:

$$\rho_0 \int_V \phi_A(z',t) d^3\mathbf{r} = f N_{BCP} n_C \tag{2.39}$$

Taking the total time derivative of both sides of (2.39), we find

$$\begin{aligned}\int_V \partial_t \phi_A(z',t) d^3\mathbf{r} &= M(\phi_A)\nabla\mu_A|_0^1 + \left(\frac{1}{\Delta L}\frac{dL_0(t)}{dt}\ \phi_A|_0^1\right) \\ &= \frac{1}{\Delta L}\left(\frac{dL_0(t)}{dt}\phi_A(1,t) - \frac{dL_0(t)}{dt}\phi_A(0,t)\right)\end{aligned}$$

Neglecting for a moment the segments convected in from the lower boundary, we evidently lose polymer segments through the free surface at a rate given by:

$$J_A(t) = \frac{1}{\Delta L}\frac{dL_0(t)}{dt}\phi_A(1,t)$$

Note that this result is not a consequence of the reference frame - applying the Leibniz rule for the derivative of the same integral (with a time-dependent upper limit L(t)) results in the same loss term.

Modifications to Conserve Polymer Segments

We propose two solutions to this problem. The first is to add a new flux term for all species at the surface equal to the loss term above:

$$\partial_t \phi_i = \nabla \cdot M(\phi_i) \nabla \mu_i + \left(\frac{1}{\Delta L} \frac{dL_0(t)}{dt} \frac{\partial \phi_i}{\partial z'} \right) + \delta_{Si} g(z') B_i \left(\phi_i - \phi_i^{eq} \right) - g(z') \frac{1}{\Delta L} \frac{dL}{dt} \phi_i (z' = 1, t)$$

The second is to introduce a velocity field that is non-zero only at the surface:

$$v(z', t) = \begin{cases} \frac{dL_0(t)}{dt}, & z' = 1 \\ 0, & z' < 1 \end{cases} \tag{2.40}$$

leading to:

$$\partial_t \phi_i = \nabla \cdot M(\phi_i) \nabla \mu_i - \frac{1}{\Delta L} \frac{\partial}{\partial z'} \left(\left(v - \frac{dL_0(t)}{dt} \right) \phi_i \right) + \delta_{Si} g(z') B_i \left(\phi_i - \phi_i^{eq} \right)$$

While this velocity field may appear pathological, a diffuse form can be derived from conservation of mass if we require that only the surface flux be compensated

by the velocity field - that is, all bulk fluid pressure is relaxed diffusively while the mass lost due to shrinking the domain is compensated by convection into the cell with the stated velocity. First, we sum the equations of motion over all monomer species:

$$\sum_i \partial_t \phi_i = 0 = \sum_i \nabla \cdot M(\phi_i) \nabla \mu_i \\ - \frac{1}{\Delta L} \partial_{z'} \left(\left(v - \frac{dL_0}{dt} \right) \sum_i \phi_i \right) + g(z') B_i \left(\phi_S - \phi_S^{eq} \right)$$

As implied previously, we assume that the Helfand compressibility penalty embedded in μ_i ensures that diffusive flow is essentially incompressible, so that $\sum_i \nabla \cdot M(\phi_i) \nabla \mu_i = 0$. Combining this with the fact that dL_0/dt has no spatial dependence, we get the following equation for the velocity:

$$\frac{1}{\Delta L} \partial_{z'} v = g(z') B_i \left(\phi_S - \phi_S^{eq} \right) \\ v(z') = \int_0^{z'} g(z') B_i \left(\phi_S - \phi_S^{eq} \right) dz$$

As $g(z') \to \delta(z' - 1)$, the computed velocity field approaches (2.40). If we assume that $\phi_S \approx \bar{\phi_S}$ over the surface region σ, then the velocity can be computed directly:

$$v(z') = B_i \left(\bar{\phi_S} - \phi_S^{eq} \right) \left(1 + \operatorname{erf} \left(\frac{z' - 1}{\sqrt{2\sigma^2}} \right) \right) \tag{2.41}$$

Regardless of the precise form for the velocity field, the only crucial feature is that $v(z' = 1) = \frac{dL_0}{dt}$ and that it decay to 0 away from the free surface. Most choices will result in violating incompressibility (unless the velocity field is closed in some consistent way, such as solving the Stokes equation with dirichlet BCs), but the Helfand compressibility penalty will relax this pressure at a rate much faster than it is generated ($\zeta N >> B_i$).

Both methods have been implemented and resolve the problem of polymer loss during evaporation simulations. All calculations reported in this thesis employed the first method, however, and this is also the method most reported in the literature. With this choice in place, all relevant aspects of the dynamical field theory methods employed here have been described. In the following two chapters, we use these tools to study the self assembly behavior of block copolymers during solvent evaporation from dilute solution and under solvent annealing conditions.

Chapter 3

Evaporation-Induced Self Assembly

Reprinted (adapted) with permission from (S.P. Paradiso, K.T. Delaney, Carlos Garcìa-Cervera, Hector D. Ceniceros, and G.H. Fredrickson, "Block Copolymer Self Assembly during Rapid Solvent Evaporation: Insights into Cylinder Growth and Stability ," *ACS Macro Letters*). Copyright (2015) American Chemical Society.

Block copolymers have emerged over the last decade as a versatile platform for a wide range of thin-film technologies including nanofiltration[1], optical coatings[32] and lithography[33]. For applications that require patterning nanoscopic pores, such as separation membranes or lithographic masks, cylinder morphologies oriented vertically ($C_\perp$) are required, but often not thermodynamically preferred. In order to meet these design constraints, researchers have turned to solvent-

mediated annealing techniques, which offer a number of advantages over conventional thermal annealing including enhanced defect annihilation kinetics and additional interaction handles for tuning film morphology[2, 5, 34–38]. Still, with the notable exception of works by Osuji and others deploying pressure-driven solvent flows[39, 40], these techniques can, at best, only mitigate the thermodynamic driving force for forming lying-down cylinders ($C_{\parallel}$), not actively promote a vertical orientation. In their seminal work, Kim and Libera [7] demonstrated that more direct influence over morphology orientation can be achieved by controlling the rate at which solvent-cast films are dried. In their experiments, the equilibrium $C_{\parallel}$ morphology was observed for modest deswelling rates ($\sim$.001mm/min), while increasing to $\sim$ .003 mm/min led to an unexpected reorientation to $C_{\perp}$ persisting over a large area. In the wake of this and subsequent work[2, 5], an expectation has developed that rapid evaporation actively drives the growth of vertical cylinders[11], which an earlier theoretical treatment appears to support[41]. More recent evidence, however, indicates that the degree of perpendicular ordering weakens with increasing evaporation rate beyond a certain threshold[6]. After over a decade of experience, there is still no consistent picture of evaporation-induced ordering in block copolymer systems. While many factors conspire to obscure the fundamental forces involved in this process, slow development is attributed in large part to the black box nature of self assembly during the solvent

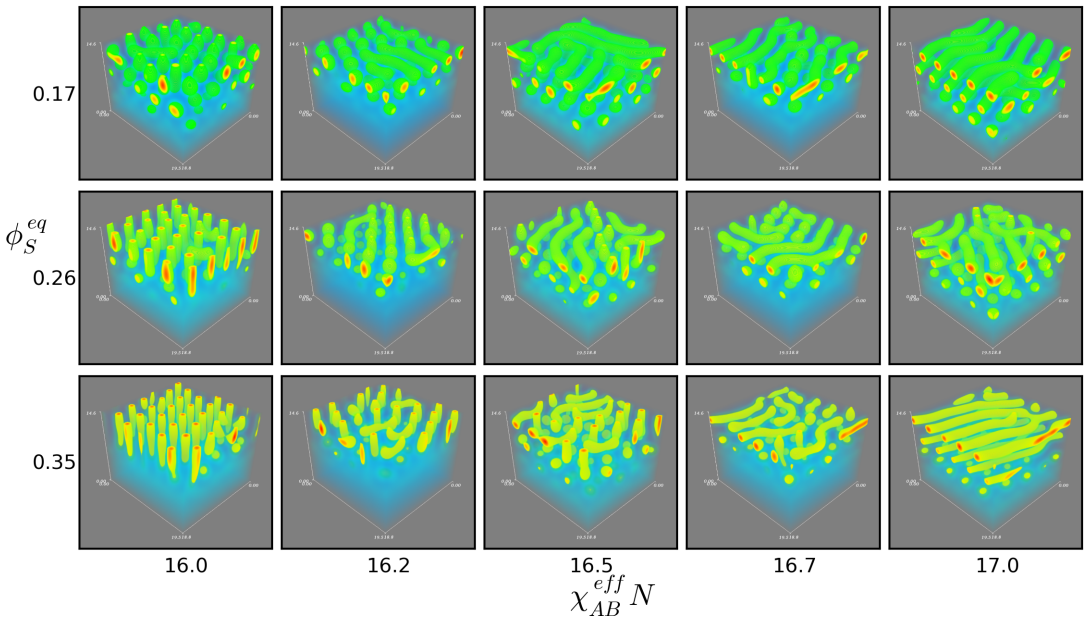

Figure 3.1: Trends in surface morphology from drying simulations. Shown are snapshots of established surface morphologies extracted from drying simulations while varying the evaporation rate through ϕ_S^{eq} and effective segregation strength through $\chi_{AB}N$. The model parameter $\chi_{AB}N$ was chosen in each simulation by inverting Eqn (3.2): $\chi_{AB}N = \frac{\chi_{AB}^{eff}N}{1.0-\phi_S^{eq}}$. Evaporation rate decreases down each column, where we see relatively minor variations in overall morphology at a given $\chi_{AB}^{eff}N$. In contrast, significant changes are observed with modest increases in $\chi_{AB}^{eff}N$. As the segregation strength is increased, the morphologies transition to primarily $C_{\|}$ surface structures through mixed intermediates. Note that only the top portion of the simulation cell is shown. The solvated polymer below the front, while containing essential solvent gradient information for the simulation, has been omitted for clarity.

removal[4]. Here, we use our dynamical self-consistent field theory framework to describe this process and provide a rational basis for designing solvent annealing systems.

Our model describes the self assembly dynamics of monodisperse diblock copolymers, comprised of chemically distinct A and B type segments in a good, neutral solvent, S. Polymers in the theory are described by continuous Gaussian chains with total length N, unperturbed coil radius $R_g \sim \sqrt{N}$, and minority A-block fraction f_A. All species in the model interact through local, Flory-type contact potentials with strength $\chi_{AB}N$, $\chi_{AS}N$, and $\chi_{BS}N$ for polymer-polymer and polymer-solvent interactions respectively[42–44].

When a droplet of dilute copolymer solution is placed in a controlled annealing chamber and exposed to solvent vapor, solvent will enter or leave the film at a rate determined by the difference in solvent chemical potential between the two phases. As solvent leaves the system with time, the total film thickness, here denoted $L(t)$, will decrease to accommodate the lost volume. A simple kinetic model, known as the Hertz-Knudsen relation[22], provides the evaporative flux (in units of $\frac{D_0}{R_g^4}$, with D_0 the monomer diffusivity) from any point $\mathbf{r}_{xy}$ on the surface as:

$$J_S(\mathbf{r}_{xy}, t) = B_i \left(\phi_S(\mathbf{r}_{xy}, t) - \phi_S^{eq}\right) \tag{3.1}$$

where $\phi_S(\mathbf{r}_{xy})$ is the local solvent fraction, ϕ_S^{eq} is the solvent fraction of a swollen film at equilibrium with the vapor phase, and B_i is a dimensionless mass transfer coefficient relating the rate of evaporative loss from the free surface to solvent

interdiffusion through the film. The latter parameters, B_i and ϕ_S^{eq}, are the variables used to control evaporation in our simulations. While this model allows for the simulation of preferential wetting conditions observed in experimental systems[38, 45], here we consider the simplest case of a neutral free surface. For the discussion that follows, we focus on asymmetric block copolymer chains that form a hexagonally packed cylinder phase at equilibrium with $f_A = 0.3$, $N = 30$, and $B_i = 5$ in order to demonstrate the interplay between evaporation rate (controlled by ϕ_S^{eq}) and segregation strength ($\chi_{AB}N$) in determining how ordering proceeds during evaporation.

3.1 Free surface morphology at the onset of ordering

We begin our discussion of the evaporation process with a visual summary of morphologies obtained from drying simulations over a range of evaporation rates and segregation strengths. We analyze the evaporation process in two parts: first, the onset of ordering at the free surface, followed by the subsequent propagation of order into the film. Importantly, the morphology formed in the initial ordering step is found to be largely determined by the solvent-mediated segregation strength at the surface of the films when ordering begins (Fig. 3.1). Note that in

the large B_i limit, fluid near the free surface rapidly equilibrates to the target solvent fraction determined by the parameter ϕ_S^{eq}. In the dilution approximation[46], the surface solvent concentration (ϕ_S^{eq}) leads to the following effective segregation strength between polymer segments:

$$\chi_{AB}^{eff} N = \phi_P^{eq} \chi_{AB} N = (1 - \phi_S^{eq})\, \chi_{AB} N \tag{3.2}$$

The results in Fig. 3.1 are organized so that the model parameters $\chi_{AB}N$ and ϕ_S^{eq} are not varied independently. Instead, the value of $\chi_{AB}N$ is set such that the derived parameter, $\chi_{AB}^{eff}N$, is held constant down each column. With this parametric constraint, much clearer trends can be discerned from the data. We find that just as $\chi_{AB}N$ dictates whether a copolymer is ordered or disordered in the melt, its solvated analogue ($\chi_{AB}^{eff}N$) is predictive of the surface morphology that develops as the films are dried. As this factor is increased, morphologies are seen to transition smoothly from primarily $C_\perp$ at the surface of the film to $C_\parallel$. Importantly, sizable changes in the evaporation rate have evidently minor effect on the pattern selection during this early ordering stage. At first, this may appear to be in disagreement with experimental evidence for ordering transitions driven by changes in the evaporation rate. However, in experimental studies, the evaporation rate is typically varied while other parameters (e.g., $\chi_{AB}N$) are

held constant. Recall from above that as ϕ_S^{eq} is lowered, the effective segregation strength increases according to Eqn (3.2). While the effects of varying the solvent vapor pressure (ϕ_S^{eq}) and $\chi_{AB}^{eff}N$ are convoluted experimentally, our simulations identify the changes in segregation strength (evaluated at the surface of the film) as the primary factor that determines pattern selection at early stages in the drying process. In order to understand this transition and how the evaporation rate impacts the propagation of order into the film, we take a closer look at the full dynamical trajectories of thin films as they are dried.

Consider the ordering trajectories illustrated in Fig. 3.2. In each case, no ordering is observed until the unstable region near the surface has penetrated a short distance ($\sim 5R_g$) into the film, allowing a single layer of phase-separated spheres to form. This is consistent with expectations derived from the mean-field phase diagram, where the path from the disordered to hexagonal phase is interrupted by a small region of FCC- and BCC-ordered spheres[44, 47]. As evaporation proceeds, the defective spheres begin to re-organize onto a hexagonal lattice. At this stage, a bifurcation appears between trajectories that lead to $C_\perp$ and $C_\parallel$ fronts. Since there is a slight time delay before ordering begins, the value of $\chi_{AB}^{eff}N$ at the surface represents how deeply the fluid is quenched into the cylinder region of the phase diagram. Systems at large $\chi_{AB}^{eff}N$ are unable to support the spherical intermediate long enough for this re-organization step to

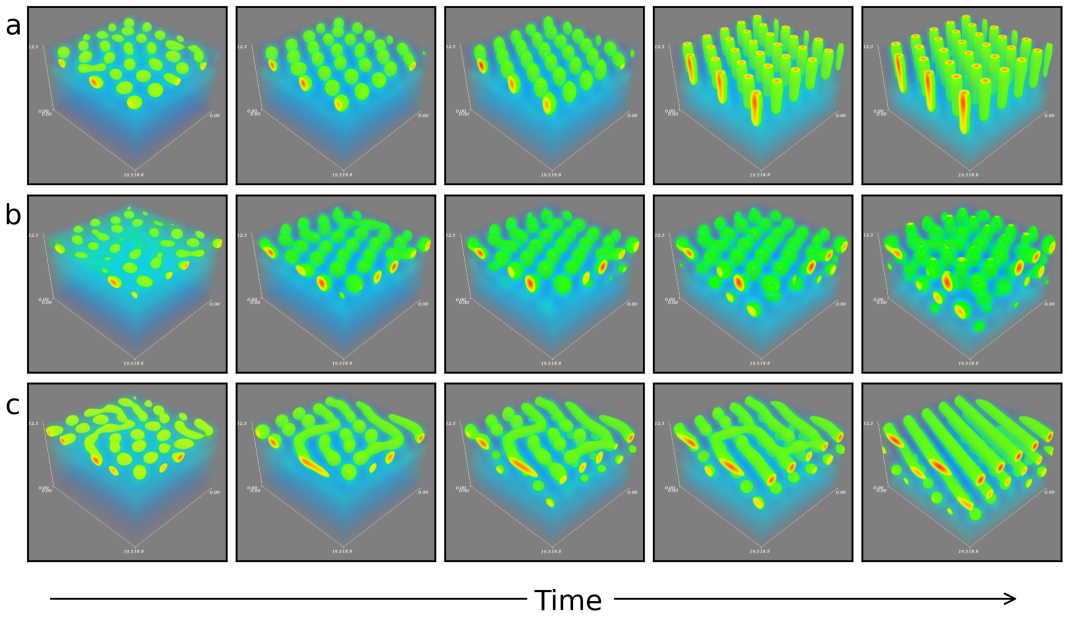

Figure 3.2: Ordering pathways in drying films. Two primary failure mechanisms deviating from the $C_\perp$ front are shown as they develop. (**a**) The typical process observed when $C_\perp$ form in drying simulations with $\chi_{AB}^{eff}N = 16.0$, $\phi_S^{eq} = 0.23$. (**b**) Increasing the evaporation rate from (**a**) by taking $\phi_S^{eq} = 0.23 \rightarrow 0.17$ leads to the formation of a second layer of spheres beneath the surface morphology, disrupting potential cylinder growth. (**c**) Increasing $\chi_{AB}^{eff}N \rightarrow 17$ leads to rapid coalescing of spheres at the surface, resulting in a $C_\parallel$ morphology. Simulation parameters (ϕ_S^{eq}, $\chi_{AB}^{eff}N$) used: (**a**) (0.23, 16.0), (**b**) (0.17, 16.0), (**c**) (0.23, 17.0).

complete, and spheres begin to coalesce to form cylinders in the plane (Fig. 3.2c). Weaker quenches, such as systems either dried more slowly or that have a lower melt $\chi_{AB}N$, provide the system sufficient time for solvent gradients to advance and spheres to stretch along the vertical axis, the first step in the transition to $C_\perp$. This accounts for the difference in behavior between Fig. 3.2a and 3.2c and

offers a simple, quasi-equilibrium explanation for why we observe a transition with increasing segregation strength.

3.2 Ordering front stability

A common frustration with solvent evaporation techniques is that while the surface morphology may show signs of hexagonal ordering (e.g., by atomic-force microscopy) the $C_\perp$ morphology often fails to penetrate the entire thickness of the film[2, 6, 38]. We observe evidence of this behavior as the $C_\perp$-forming system above (Fig. 3.2a) is pushed to a higher evaporation rate (Fig. 3.2b). Under these more rapid drying conditions, the surface morphology fails to establish a coherent front. Instead of growing to form $C_\perp$, the initial surface morphology pinches off from the front as a new layer of spheres begins to form. This is a critical observation, as it is often assumed that once order is established at the free surface, the advancing front will act as a chemical pre-pattern with which drying fluid may fall into registry. Instead, simulations undergoing rapid evaporation consistently feature a secondary growth mode that competes with the initial patterning at the surface.

This behavior can be explained by considering the microscopic details underpinning our field theory. To this end, it is helpful to compare the ordering fronts

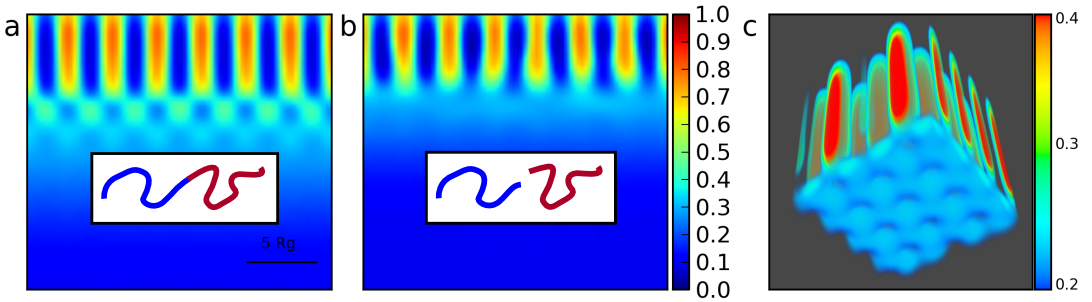

Figure 3.3: Bonding constraints emerge destabilizing patterns beneath the front. (**a**) Drying simulations of a symmetric block copolymer ($f_A = 0.5$) system exhibit a regularly patterned response layer at the interface between ordered and disordered fluid. (**b**) When these simulations are repeated with a symmetric homopolymer blend, no response layer is observed. (**c**) Ordered $C_\perp$ front (upper, red) and response layer (lower, light blue) from an evaporation simulation of $f_A = 0.3$ diblock copolymers in 3D, seeded with an initially perfect $C_\perp$ structure for illustration. Note that the density scale has been modified in order to visualize the response layer.

formed beneath solvated homopolymer blend (Fig. 3.3a) and symmetric diblock copolymer (Fib. 3.3b) films. In the case of connected diblock copolymer chains, the perfect ($L_\perp$) pattern in the surface region does not lead to a coherently ordered response layer in the wet film. Rather, a sequence of half-period shifts is observed to bridge the transition from the ordered plug to the disordered polymer beneath the front. We believe these shifts are physical in nature and originate from the self-exclusion phenomenon known as the correlation-hole effect in the scattering theory of block copolymer melts[44, 48]. The correlation-hole emerges from the combination of local segment-segment repulsion and the molecular bonding constraint, leading to density correlations on length scales comparable to the

random coil radius, R_g. At a patterned interface, these density correlations seed the secondary structures observed in our simulations. Notice that severing the bonding constraint (Fig. 3.3a) and preparing an equivalent homopolymer blend results in loss of structure at the front, confirming that its presence in the diblock case is a direct consequence of the copolymer chain topology. This correlation-hole effect is particularly disruptive for achieving $C_\perp$ order. While the response region attracted to the leading edge of a $C_\parallel$ front is compatible with lying-down cylinders, the pattern formed beneath an array of vertical cylinders (Fig. 3.3c) will not admit simple propagation of $C_\perp$ into the film. However, understanding the presence and origin of these disruptive patterns may allow us to devise formulation adjustments that mitigate their effect.

While the qualitative comparison between the diblock the homopolymer blends offers a strong case for block connectivity being the origin of these correlated fluctuations at the front, we can probe this relationship more rigorously. Expressed another way, the arguments above amount to the suggestion that the disordered, near-critical fluid just beneath the ordered region of the film at the far edge of the ordering front is slightly more susceptible to fluctuations that are *anticorrelated* with the composition of the ordered fluid. If true, then it follows that at any point in time, we are more likely to observe concentration fluctuations of the opposite sign as the ordered fluid above, a statistical signature that can be measured by

the following correlation function:

$$\begin{aligned} A(\delta z) &= \frac{\langle \psi(x, z_0, t)\psi(x, z_0 + \delta z, t)\rangle_{x,t}}{\sigma_{\psi(z=z_0)}\sigma_{\psi(z=z_0+\delta z)}} \\ \psi(x, z, t) &= (\phi_A(x, z, t) - \phi_B(x, z, t)) \\ &\quad - (\phi_A(x, z, t) + \phi_B(x, z, t))\,(2f_A - 1.0) \end{aligned} \tag{3.3}$$

This information is, in principle, accessible through a generalization of the standard Random Phase Approximation (RPA) analysis[29]. In the RPA, the mean-field Hamiltonian is expanded to second order in density fluctuations about a spatially homogeneous state:

$$\beta\widehat{H} = \frac{1}{2}\int d^3\mathbf{k} \sum_{ij} A_{ij}(\mathbf{k})\delta\phi_i(\mathbf{k})\delta\phi_j(-\mathbf{k}) + \ldots \tag{3.4}$$

and the correlation function can be calculated from the statistical mechanics:

$$\begin{aligned} \langle \delta\phi_i(\mathbf{k})\delta\phi_j(-\mathbf{k})\rangle &= \int \mathcal{D}\delta\phi(\mathbf{k})\ \delta\phi_i(\mathbf{k})\delta\phi_j(\mathbf{k})\frac{e^{-\beta H}}{\int e^{-\beta H}} \\ &= A_{ij}^{-1} \end{aligned} \tag{3.5}$$

where the last equality follows from the second moment of a multidimensional Gaussian distribution, equal to the RHS by construction after expanding to second order in the composition fluctuation. However, the density response relevant to the correlations of interest in our system, during evaporation, is no longer a per-

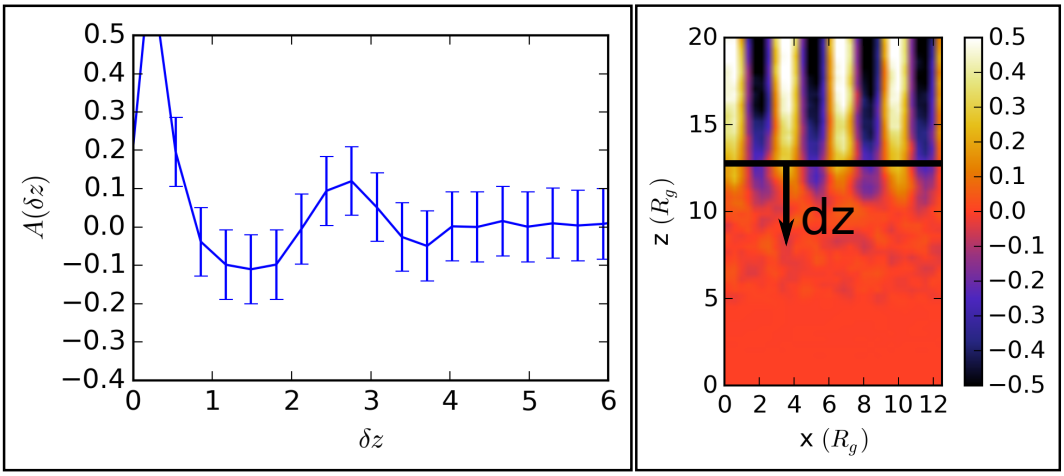

Figure 3.4: The compositional auto-correlation function between the ordering front and the ordered plug near the free surface is shown (left) alongside a snapshot of the steady-state evaporation system used for the calculation (the order parameter $\psi(x, z, t)$, defined in the text, is shown). The curve was generated for a symmetric A-*b*-B diblock with $f_A = 0.5$ with $B_i = 0.3$, $\chi N = 17$, and $\phi_S(z = 0, t) = 0.6$.

turbation from a spatially homogeneous state, rendering the required calculation analytically intractable.

In order to sample the correlation statistics numerically, we must track the correlation function in (3.3) over the course of an entire evaporation simulation. This approach is cumbersome, however, due to the fact that the location of the front is not stationary. In order to collect statistics on the correct quantity, an ensemble of drying trajectories would have to be run and the correlation function averaged over simulation instance rather than time. In order to dramatically improve our sampling statistics, we instead simulate a *steady-state* ordering front by enforcing a fixed concentration dirichlet boundary condition at $z = 0$ on the

solvent concentration and allowing solvent to evaporate from the free surface by the standard mechanism. After a brief equilibration period, this results in a steady state with ordered polymer near the free surface and a solvent concentration profile that increases with distance from $z = L_z$. Following this procedure, a system was prepared with $f_A = 0.3$, $N = 30$, $\chi_{AB}N = 17$, and $B_i = 0.3$ and simulated with thermal fluctuations ($C = 1500$). Figure 3.4 shows the result of averaging equation (3.3) over approximately 83 correlations times using a reference $z_0 = 12.5R_g$.

At $\delta z = 0$, the correlation function assumes a large value consistent with the fact that the ordered region does not change structure significantly over time. Note that the autocorrelation function being reported is resolved over spatial distance, not temporal distance, yet the appropriate normalization is the local fluctuation strength (averaged over time). This is the reason $A(\delta z = 0) \neq 1$. Otherwise, the same intuition for autocorrelation applies in that the function will decay to 0 with distance from the ordering front as we expect the fluctuations to become uncorrelated deep in the disordered state. What happens between those extremes, however, is of great interest as it tells us about how the pattern at the front imprints a pattern in the near-critical fluid that is about to microphase separate and join the ordered region as solvent continues to evaporate. Three options appear likely *a priori*. First, the correlation function may simply decay

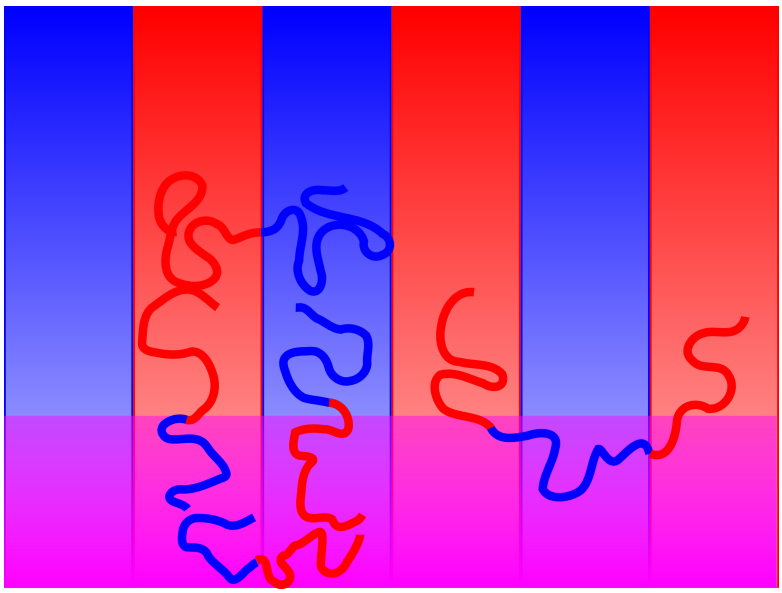

Figure 3.5: A schematic illustration of the chain conformations consistent with the observed bias in composition fluctuations at the ordering front. For diblock chains, the dangling chain ends from the lamellae must stretch significantly to either side in order to stay consistent with the original pattern. As a consequence, composition fluctuations consistent with the a single shift in the lamellar period are slightly preferred. Triblock chains, however, sample an additional set of bridging conformations that are consistent with the original pattern. The entropic contribution from these configurations may dampen the response layer.

monotonically to 0 with distance from the front. If the correlation length were long, this would suggest that the pattern is communicated into the disordered region and that we should expect this pattern to propagate reliably into the film. Alternatively, the correlation function could be structured to reflect the molecular size of the underlying chains and the length scale associated with the correlation-hole ($\sim R_g$) but the composition fluctuations feature positive correlation near the front. In fact, we see the opposite. Consistent with the response layer that appears in our drying simulations, the autocorrelation function clearly features an anticorrelated layer on the disordered edge of the ordering front. In order to understand this result, it is useful to consider the possible chain conformations that would be consistent with the two patterns (both correlated and anticorrelated with the ordered plug). These are schematically illustrated in Figure 3.5. Deep in the lamellar domains, the chains are strongly polarized and orient parallel to the free surface. As the chains approach the ordering front, this polarization weakens and A-block segments at the interface associate with the A-rich lamellar sheets while the attached B-block segments are left dangling at the interface. This conformation is the dominant one we suggest is the physical origin of the response layer observed in our calculations. In order for the dangling chain ends to associate with neighboring stripes of the same monomer color, the diblock chain would have to stretch to either side and incur unfavorable stretching entropy penalties. This

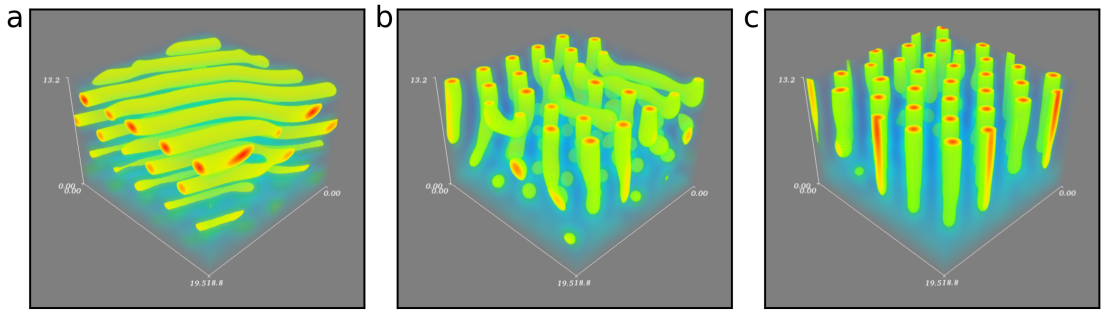

Figure 3.6: Selective solvent stabilizes $C_\perp$ by weakening the correlation-hole. Solvent quality for the majority block increases from left to right. Since the pre-pattern present at the leading edge of a $C_\perp$ front is rich in the minority block, a solvent that preferentially swells the majority block inhibits the growth of this mode and enhances the stability of the front. Selectivity is measured by $\Delta\chi_S N = \chi_{AS}N - \chi_{BS}N$, increasing from left to right: (**a**) -7, (**b**) 0, (**c**) 7.

implies a novel vector for considering the influence of chain architecture on the stability of the ordering front. For triblock copolymer chain architectures, one may expect that the added contribution from bridging conformations would act to dampen the response and stabilize the front.

We conclude with another promising result on the stabilizing effect a majority block-selective solvent has in our simulations. As shown in Fig. 3.6, sweeping the solvent selectivity from weakly favoring the minority to majority block species has a pronounced effect on the quality of vertical cylinders obtained during evaporation. While a rigorous connection remains elusive, it is tempting to explain this behavior in the context of the correlation-hole phenomenon described above. As evident in Fig. 3.3c, the destabilizing response layer (light blue in the figure)

beneath vertically oriented cylinder fronts is rich in polymer segments of the minority block. We suggest that the majority block-selective solvent may be acting to penalize the formation of this response layer, resulting in the enhanced stability observed in our simulations. We note that within the limited data available, majority block-selective solvents have been seen to correlate with perpendicular cylinder formation in drying experiments [2].

3.3 Conclusions

This work has provided the first opportunity to visualize block copolymer self assembly under rapid evaporation conditions. Our simulations indicate that the resulting morphology depends strongly on the effective segregation strength, $\chi_{AB}^{eff}N$, near the surface of the film. When films are dried too rapidly, however, even modest surface segregation strengths fail to achieve stable growth of $C_{\perp}$, owing to a dynamical instability observed at the ordering front. Tracing the origin of this instability to the correlation-hole opens up exciting new opportunities for guiding the self-assembly process, such as including selective solvents or blend additives that have been shown to weaken correlations observed at the front[49]. Given this understanding, it would be of interest to examine whether chain architecture, which is at the heart of these competing correlations, can be exploited to

promote desired ordering pathways. For the cylinder-forming system, we predict that an asymmetric triblock polymer whose midblock is the *minority* component may feature a much more stable ordering front due to contributions from bridging conformations. While we have focused on the problem of aligning vertical cylinders, this work illustrates fundamental aspects of ordering during solvent evaporation, which may prove essential for understanding evaporation-induced self assembly in broader classes of nanostructured soft materials.

Chapter 4

Cyclic Solvent Annealing of Block Copolymer Thin Films

Reprinted (adapted) with permission from S.P. Paradiso, K.T. Delaney, C. Garcìa-Cervera, G.H. Fredrickson, "Cyclic Solvent Annealing Improves Feature Orientation in Block Copolymer Thin Films " *Macromolecules, Submitted*. Copyright (2015) American Chemical Society.

Practically since its discovery, the self assembly of block copolymers into regularly spaced nanostructures has inspired materials scientists to seek reliable methods for controlling the formation of these nanoscale features. That block copolymer thin films are actively being considered as template materials for demanding lithography applications in semiconductor devices[50, 51], storage media[52, 53], and others[9, 11, 54], where precise control over domain orienta-

tion and placement is critical, stands as a testament to the significant progress made in this area. However, challenges remain for systems in which either the choice of monomer chemistry or polymer molecular weight motivates the use of solvent annealing techniques in order to obtain well ordered films. These challenges rest primarily in our poor understanding of the morphology dynamics that occur as films are swollen, annealed, and dried, where evidence exists for nontrivial morphology changes occurring at each stage[4, 55, 56]. In addition, many promising commercial applications, such as copolymer membranes for ion exchange or ultrafiltration[3], demand strict control over feature orientation. For copolymer filtration membranes based on a self-assembled cylinder motif, pores connecting each side of the film must be uniformly oriented across macroscopic length scales to avoid pore-closing defects or parallel domains limiting flux across the film.

While many methods have been developed to produce oriented block-copolymer domains[57–60], each imposes limitations on either the scalability of the process or choice of monomer chemistry. Electric fields have been shown to effectively orient lamellae by exploiting the dielectric contrast between the separated domains, but these methods, as well as those that employ magnetic fields[59], necessarily add constraints on the monomer chemistry that can be used and possibly entail expensive or impractical changes in equipment for large scale manufacturing. For these reasons, methods focused on using solvent annealing and evaporation to drive the

oriented growth of block copolymer structures continue to show promise. The added flexibility afforded by the choice of solvent system is essential for accommodating a variety of monomer chemistries and surface conditions, and suggests a viable route to continuous roll to roll production of nanostructured polymer materials. Unfortunately, the slow kinetics of self assembly of long polymer chains, combined with the gradually diminishing solvent gradients during evaporation, often lead to decoherent ordering fronts in evaporation-induced self assembly methods, which result in narrow processing windows for viable "one shot" methods to cast films with vertically oriented features using solvent evaporation alone[6, 17].

Here, we report a new approach that seeks to build on these strategies, while simultaneously optimizing the rate and reliability of forming vertically oriented features by focusing on the swelling/deswelling process as a mechanism for pattern selection. While notably not the case for the sphere or complex network phases, both the industrially relevant lamellar and cylinder phases feature solid-like behavior in response to strain along at least one axis while admitting continuous deformation in the other(s) at little to no cost in elastic free-energy. Modulating the thickness of thin copolymer films is a well-known method for exploiting this behavior to penalize the formation of parallel features, but as the strain is distributed across all $n = \left(\frac{L}{L_0}\right)$ periods, the free-energy penalty weakens with increasing film thickness. Instead, we focus on a controlled swelling process that

guarantees continuous strain of defect features oriented parallel to the substrate across the entire swell cycle. Importantly, since swelling with a specified concentration of solvent results in a total strain proportional to the dry dimensions, the method preserves its effectiveness as the film thickness is increased. In addition, the swelling process broadens the set of kinetic routes to defect annihilation by relaxing the constraint of constant volume across the annihilation event. It has been demonstrated that significant morphological development, including full reorientation, can be observed as polymer films swell with solvent [55].

In this chapter, we discuss how cycling films by repeatedly swelling with a neutral solvent produces morphologies with a high degree of vertical orientation and enjoys favorable kinetics when compared with thermal cycling or static solvent annealing. Further, the benefits are shown to emerge only after multiple cycles, offering a possible explanation for why this method has not been previously explored. Our approach is motivated in part by a growing awareness for the importance of kinetics in block copolymer self assembly and the utility of dynamical simulations to understand the connection between processing conditions and material structure and properties[4, 24, 61]. In order to isolate and understand the role of solvent swelling in defect annihilation, we apply a dynamical field theory method to investigate controlled comparisons between three different annealing scenarios under analogous conditions: static solvent, cyclic solvent,

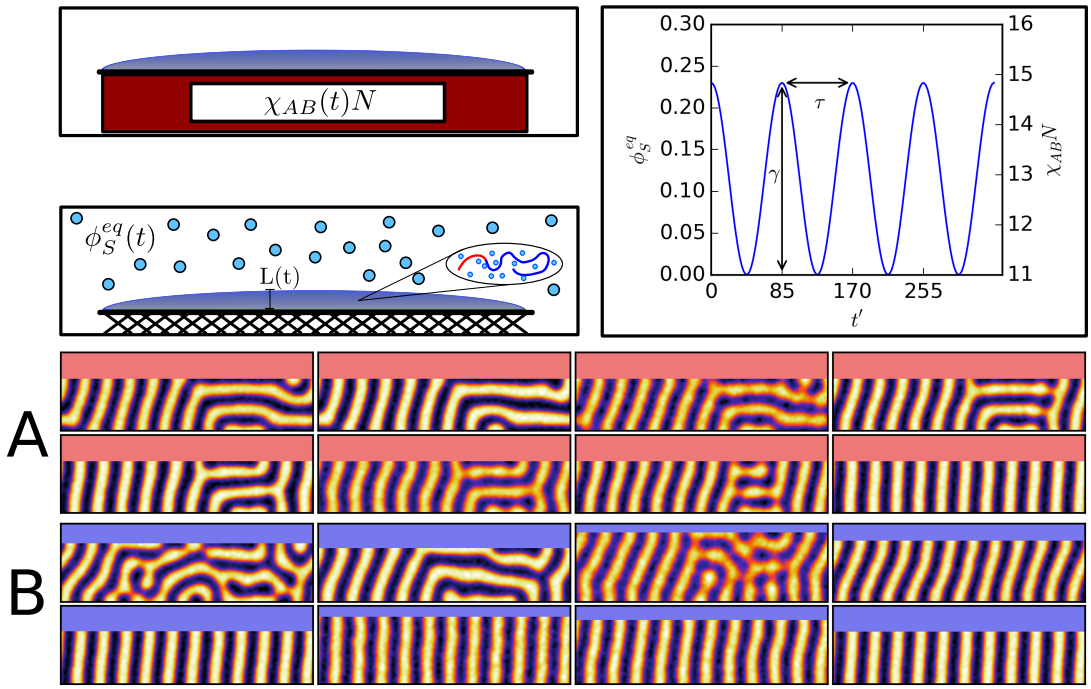

Figure 4.1: Illustration of the cyclic thermal (A) and cyclic solvent vapor annealing (B) procedures from 2D simulations with $N = 100$, $B_i = 1.1$, $\tau = 85$, $\chi_{AB}N = 17$, $\gamma_{CSVA} = .23$, $\chi^0_{AB}N = 13.1$, $\gamma_{\chi_{AB}N} = 3.9$, $C = 2500$, and $f_A = 0.5$ following the cyclic annealing schedule plotted above. Simulation time increases from left to right, top to bottom in the image sequence and is the same for each series: $t' = 49, 74, 99, 124, 149, 174, 199, 224$, corresponding to 3 full cycle periods.

and cyclic thermal annealing. In this way, contrast between the results of different methods can be rigorously connected to the few, controlled differences in simulated annealing procedure.

4.1 Cyclic solvent annealing method

Consider a thin copolymer film placed in an annealing chamber and exposed to a controlled solvent atmosphere. Following time $t = 0$, the partial pressure of the solvent in the chamber is varied (through manipulation of inlet gas streams, for example) to produce the following oscillatory annealing conditions:

$$\phi_S^{eq} = \phi_S^{min} + \frac{\gamma}{2}\left(\cos\left(\frac{2\pi}{\tau}t'\right) + 1\right). \tag{4.1}$$

We note that the period of this oscillating surface solvent concentration, τ, has been nondimensionalized in units of the Rouse time, τ_p. It is worthwhile to consider the time scales present in the dynamics model as there are now four ostensibly distinct quantities. These time scales include the time $\tau_k \sim \frac{R_g}{kaP_S^{sat}}$ for the free surface concentration to equilibrate after a change in ϕ_S^{eq}, the solvent inter-diffusion time $\tau_S \sim \frac{R_g^2}{D_0}$, the polymer chain relaxation (Rouse) time $\tau_p \sim \frac{NR_g^2}{D_0}$, and the cycle period τ. We will show later that the cyclic solvent annealing method performs well in the regime where $\tau > \tau_p$, which is essential since our density dynamics are accurate only when considering time scales larger than τ_p[16]. Without good estimates for the mass transfer coefficient to the surface, k, it is unclear whether the ratio $\tau_S/\tau_k = B_i >> 1$ such that the free surface concentration becomes slaved to $\phi_S^{eq}(t)$. However, it is simple to reason through

the consequences of each regime in order to rationalize the assumptions with experimental data. If $\tau_k/\tau_S >> 1$, then no solvent gradients will persist across the film and the film thickness will asymptote exponentially to its equilibrium value as $\frac{\Delta L(t)}{\Delta L_{max}} = 1 - \exp(-\alpha t)$, therefore exhibiting a swelling rate $\frac{\Delta L(t)}{\Delta L_{max}} \sim \alpha t$ for small t after a step change in ϕ_S^{eq}. In contrast, if solvent uptake were limited by internal diffusion, the solvent profile would follow the well-known error function solution and film thickness would increase at a rate proportional to $\sqrt{t}$[62]. Experiments on polystyrene-*b*-polybutadiene thin films swollen with a neutral solvent (chloroform) demonstrated that the swelling behavior followed the latter scenario, consistent with a rapid equilibration of the solvent concentration at the free surface followed by Fickian diffusion into the film[63]. As will become apparent later, this assumption is not essential for the benefits of cyclic solvent annealing to be realized; however it simplifies the comparison with cyclic thermal treatment and so we focus on this regime.

As the solvent fraction in the film is varied across the cycle, two critical thermodynamic forces in the system are altered. First, it is well known that the effective segregation strength driving phase separation is reduced in the presence of a neutral solvent, the effect of which is captured by the dilution approximation: $\chi_{AB}^{eff} = \chi_{AB}\phi_P^{\alpha}$[64]. In SCFT, $\alpha \approx 1$ for neutral solvents, provided the solvent concentration is spatially homogeneous[65], although the value has been

postulated theoretically[66, 67] and shown to vary experimentally, especially near the ODT where α takes on values between $1.3 - 1.6$[68]. Second, the swelling of the film, which occurs primarily in the thickness direction due to contact line pinning, leads to an elastic strain on features oriented parallel to the substrate that requires chains to stretch in order to accommodate the expanded domain. For large swelling amplitudes, as the domain continues to expand, the free-energy of these features will increase in relation to both the disordered and vertically oriented states, thus lowering or eliminating the barrier to melting and reorienting. These two effects together serve to accelerate the reorientation of parallel features during the first half of the cycle. Indeed, in our simulations, most defect annihilation events are observed as defects are strained under extension during the swell step. During the de-swell step, $\chi_{AB}^{eff}N$ increases, leading to sharpened interfaces and solidifying the new structure with statistically fewer parallel features than the previous cycle. Many of these effects associated with lowered segregation strength and enhanced defect annihilation kinetics near the ODT have been discussed in the literature[4, 61]. The isolated influence of film swelling alone, however, is an essential ingredient, which can be seen by comparing simulations of cyclic solvent annealing with a film cycled only in temperature, where the film thickness is held

constant, but the segregation strength varies in time as:

$$\chi_{AB}(t)N = \chi^0_{AB}N + \gamma/2\left(cos\left(\frac{2\pi}{\tau}t'\right) + 1\right). \tag{4.2}$$

An illustration of these two processes is shown in Figure 4.1. Here, a sequence of polymer segment concentration fields (species A) is shown across two full annealing cycles. In the thermal annealing sequence, a representative defect annihilation pathway is observed. First, the as-cast system naturally anneals into a mixed state containing parallel and vertically oriented lamellar features separated by a stable grain boundary. Upon heating, the disordered state begins to compete with the meta-stable defect at the grain boundary and fluctuations ultimately cause a short section of the parallel region to reorient, moving the grain boundary in towards the center by one full lamellar period. Upon heating the second time, now adopting an improved state from the previous cycle, the grain boundaries diffuse towards the center of the cell, through another thermally activated sequence to heal the interface, resulting in a uniform array of vertically oriented lamellae. In contrast to the discrete single-period healing steps during thermal treatment, the strain experienced by the parallel features during cyclic solvent vapor annealing (CSVA) leads to spontaneous melting of the morphology in the parallel region, which subsequently reforms into stable vertical stripes prior to de-swelling. While

clearly illustrating the key features that distinguish the CSVA method, this example is unrepresentative in two respects. First, the simulated trajectory was such in the CSVA case that all defects were removed in a single cycle. When multiple trajectories are sampled and averaged, as shown below, full orientation is on average observed after 3 full cycles, not 1. Second, the as-cast film happened to have a thermally accessible state with perfect vertical alignment of domains so that the kinetic process could be compared between the two methods. In practice, at the conditions considered in this paper, cyclic thermal annealing trajectories that result in perfectly oriented features prove to be the minority of cases.

To quantify the effect that cyclic solvent annealing has on the orientation of block copolymer domains, we introduce an orientational order parameter based on the local nematic director from the study of liquid crystals[69]:

$$\begin{aligned} n_i(r) &= \frac{\left(\nabla \rho_A(\mathbf{r},t)\right)_i}{|\nabla \rho_A(\mathbf{r},t)|}, \\ Q_{ij}(\mathbf{r}) &= \left(n_i n_j - 1/d\right). \end{aligned} \tag{4.3}$$

where d is the dimensionality of space and a normalized of the concentration gradient takes the place of the director field. Since we are interested solely in vertically oriented features, we define our order parameter to select the xx component of Q_{ij} (x varies along the lateral dimension of our film):

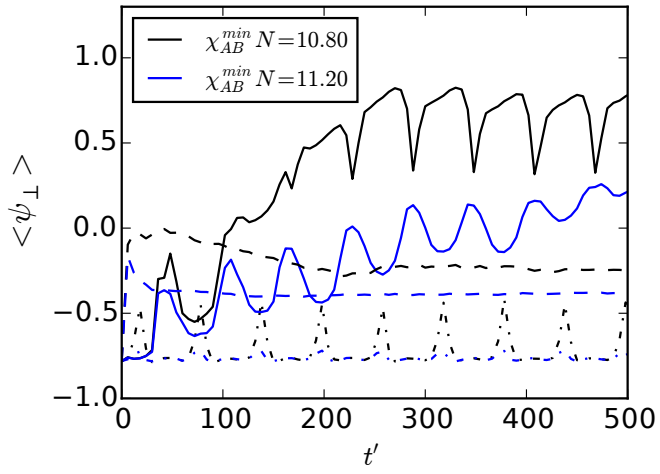

Figure 4.2: The value of the orientational order parameter (defined in the text) as a function of time for two cycle amplitudes $\chi_{AB}^{min} N$, defined as the smallest effective segregation strength experienced during the annealing cycle. Three annealing strategies are compared: cyclic solvent annealing (-), static solvent annealing (--), and cyclic thermal annealing (-.-) for lamellar forming as-spun films cast at an incommensurate film thickness $L = 3.5L_0$, $N = 100$, $\tau = 80$, $C = 2500$. Each trace is an ensemble average of 30 independent simulation trajectories.

$$\psi_\perp(t) = \frac{1}{V} \int a Q_{xx}(\mathbf{r}, t) d\mathbf{r}, \tag{4.4}$$

where $a = 2$ in 2D and $a = 3/2$ in 3D so that $\psi_\perp(t)$ varies continuously between (-1, 1) with $\psi_\perp = -1$ corresponding to a film with uniform parallel orientation of lamellar domains and $\psi_\perp = 1$ corresponding to perfect vertical orientation.

We first apply this analysis to compare simulations of cyclic thermal, cyclic solvent, and static solvent annealing of thin films (Fig. 4.2). All calculations were performed in 2D in order to generate a sufficient number of dynamical trajectories

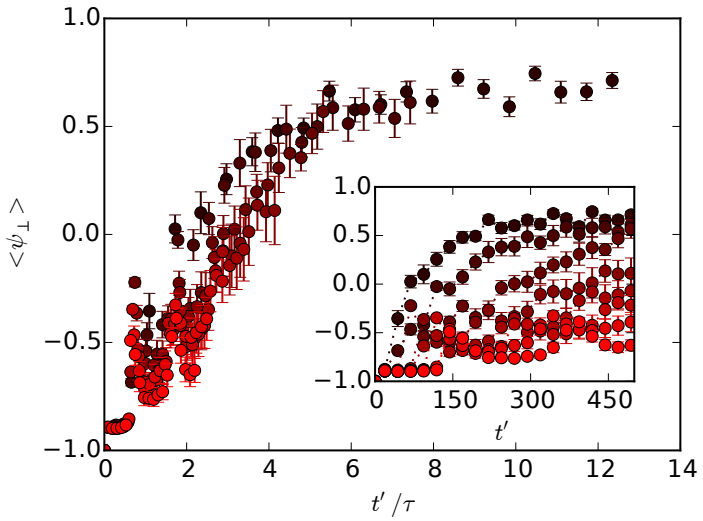

Figure 4.3: Orientational order parameter for 2D simulations of lamellae from CSVA simulations as a function of time, for multiple cycle periods ($\tau = 40, 66, 92, 119, 145, 172,$ and 198). Each trace is an ensemble average of 30 independent trajectories with $f_A = 0.5$, $N = 100$, $L_x = 29R_g$, $L_z^{dry} = 10.7R_g$, $C = 2500$, and $\chi_{AB}N = 14.5$.

to produce meaningful statistics. We acknowledge that, by restricting our focus to 2D kinetics, we necessarily limit the expression of certain kinetic pathways available to the system, but the primary impact of strain asymmetry is captured and focused on here. Despite setting the initial film thickness to be strongly incommensurate with parallel lamellae, neither the films that underwent χN cycling nor the solvent annealed films were strained sufficiently for a thermally activated reorientation event to be observed during the time it took for the films cycled with solvent to achieve nearly perfect orientational order. Note that while the theoretical maximum value $\psi_\perp = 1$ is never realized, the discrepancy observed is

due to slanted, but otherwise vertically oriented features, where slanting is likely a consequence of slow relaxation combined with lateral incommensurability of the simulation domain.

Evidently, increasing focus on the swelling process has a positive impact on the selection for vertical order in annealed thin films. While solvent annealed films, featuring a single swell/deswell cycle, performed worse than those cycled with solvent, both methods featured higher average selection for vertical orientation than thermal cycling. However, the CSVA process introduces an additional parameter, the cycling period τ, which must be tuned for optimal performance. Clearly, if performance is sensitive to this parameter, then the method may be restricted in practice to a narrow range of experimentally accessible values. Figure (4.3) shows data from an ensemble of cyclic solvent vapor annealing calculations across multiple cycle periods (τ). While results differ significantly from one trajectory to another, the average time-series $\psi_{\perp}(t)$ taken over 30 independent simulations converges to a consistently improving trend of orientational order with annealing time. Notably, the convergence rate to perfect vertically oriented domains slows as the cycle period is increased; however, the data collapse when the time-series is plotted against the reduced time t'/τ. This behavior reinforces the importance of the total accumulated strain in the swell/deswell process to the performance of cyclic annealing as orientational order improves not strictly with annealing

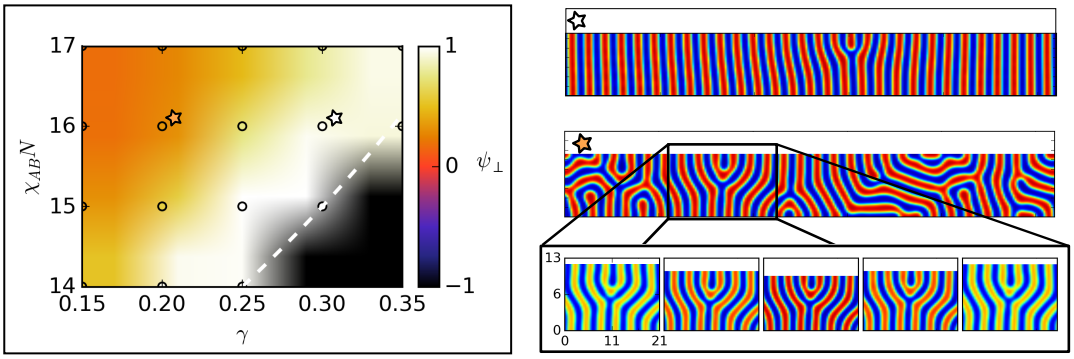

Figure 4.4: The degree of vertical orientation after 4 full swell/de-swell cycles as a function of the maximum strain amplitude (γ) and melt segregation strength ($\chi_{AB}N$). The mean-field order-disorder transition line at the height of each swell cycle is provided for reference (dashed white). Polymer segment concentrations are shown to the right, one taken from the perfect ordering band (top) and the other from the understrained band (middle). The under-strained morphology features a number of steady-state defects, one of which (an elementary dislocation) is highlighted across a single cycle period. Calculations were run with $C = \infty$, $N = 100$, $f_A = 0.5$, $\tau = 250$.

time, but is more directly correlated with the number of completed cycles. Finally, it is worth noting that while rapid cycling rates ($\tau < 100$) enjoyed superior convergence to perfect ordering than the data-collapsed universal behavior, these demand rapidly varying annealing conditions that are unlikely to be realized in experiment. However, the balance of the data indicates that performance does not degrade with increasing cycle period over the range accessible to our simulations, suggesting that cycling itself should be sufficient to improve orientational order without targeting a narrow band of optimal τ.

4.2 Operating windows for cyclic solvent annealing

It is essential for any successful annealing strategy to provide not only a path to the desired state, but also for the process to possess broad operating windows and thereby avoid strict limits on allowed uncertainty in experimental conditions. To test the robustness of the proposed cyclic solvent annealing method, we have evaluated its performance across a range of block segregation strengths ($\chi_{AB}N$) and swell fractions (γ), summarized in Fig.(4.4). Note that in this set of calculations, a slightly modified annealing schedule was implemented in order to simulate a more realistic swelling procedure. In place of the single harmonic oscillating target given in (4.1), the value of ϕ_S^{eq} was set to alternate periodically between 0 and γ, switching when the average solvent profile reached less than 1% offset from its equilibrium value. The τ reported in Fig. 4.4 is the average observed time between switching. This method more closely approximates an experimental system where the atmosphere is periodically evacuated and replaced with dry or wet air. Each point in the map represents the final value of the perpendicular order parameter, $\psi_\perp$, after a single deterministic large-cell 2D calculation run for 4 complete cycles, at which point the map separates into 3 distinct regions: under-strained (small γ, large $\chi_{AB}N$), perfect ordering (mild γ, mild $\chi_{AB}N$), and overstrained (large

γ, small $\chi_{AB}N$). Behavior in the overstrained region is relatively straightforward to understand. This regime is bounded by the order-disorder line, beyond which the morphology melts completely between cycles, losing all memory of the former structure. In the central band, we find a region of approximately constant width bounded by the ODT line on the right and a ($\chi_{AB}N$-dependent) minimum swelling fraction on the left, bounding an operating window for achieving perfectly uniform vertically oriented lamellae. We note that over the range of parameters accessible in our study, the shape of the ideal operating window stays approximately constant after broadening from the small $\chi_{AB}N$ limit. Finally, below a critical strain amplitude, a steady-state population of dynamically stable defects emerge that persist through further cycling. Interestingly, these typically occur as point defects in our 2D calculations, although it is unclear whether isolated sphere or line defects would form predominantly in 3D. We frequently observe these defects embedded within vertically oriented features that are able to alleviate the strain due to swelling at minimal cost in free-energy. Ultimately, the dissolution of these isolated defects must be accomplished through thermal events and are not accelerated significantly by the cyclic annealing process.

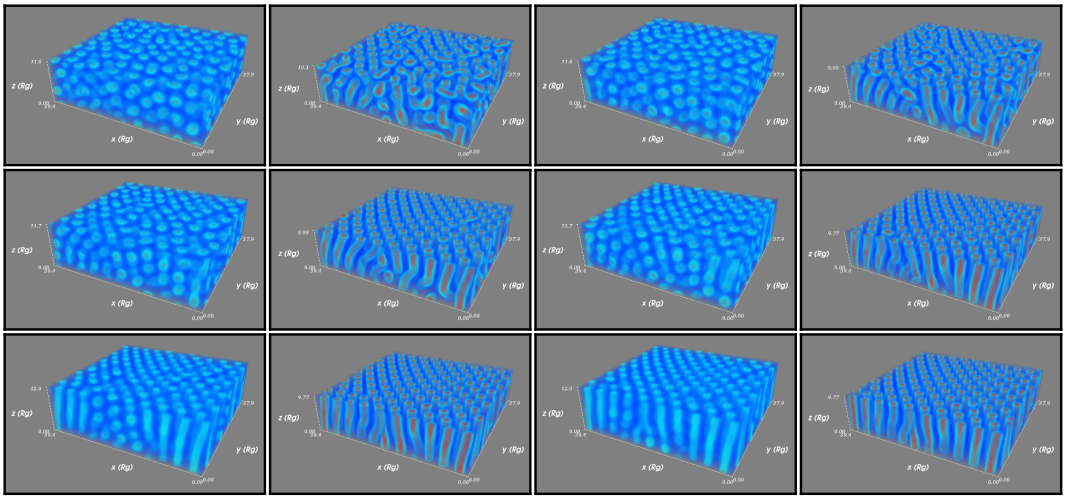

Figure 4.5: Density snapshots from a cyclic solvent vapor annealing simulation of a cylinder-forming BCP system with $f_A = 0.3$, $\tau = 50$, $N = 100$, $C = 10000$, $\gamma = 0.2$, $\chi_{AB}N = 18.125$. Time increases left to right, top to bottom: t' =47, 72, 97, 122, 147, 172, 197, 222, 247, 272, 297, and 322.

4.3 Cylinder-forming thin film results in 3D

All of the results presented so far have focused on 2D lamellar-forming BCP films. However, the selection mechanism based on anisotropic strain we have suggested applies equally well to cylinder-forming BCPs. Indeed, calculations with an asymmetric BCP ($f_A = 0.3$) readily yield highly ordered thin films with uniform, vertically oriented features (Fig. 4.5). However, the 3D calculations feature an additional mechanism unavailable to the lamellar system for encouraging long range order. This is due to the order-order transition from cylinder to sphere morphologies that occurs when a critical solvent concentration is reached at the

height of a swell cycle. Unfortunately, the expense of 3D calculations with simulation cells large enough to avoid finite size effects restrict the range of cycle periods accessible. In simulations at this outer limit, dictated by our computational resources ($\tau = 50$), we found that cylinders embedded within defect free domains were more stable at strong swelling than regions with defects. That is, under the conserved diffusive dynamics employed here, perfectly aligned vertical cylinders decompose into spheres upon swelling with solvent more slowly than do cylinders placed under strain by nearby grain boundaries or defects. This resulted in selective melting of poorly ordered regions, systematically improving the order of the thin film with increasing swell/deswell cycles. The rapid cycling rate, while notably much slower than the single chain relaxation time, but faster than the order-order transition for the spheres to reorganize onto a cubic lattice, caused spheres in poorly ordered regions to coalesce vertically into increasingly well ordered arrays of cylinders during the deswell step. To bring this cycle period into reference, assuming $D_0 = 10^{-10} cm^2/s$, $R_g = 10nm$, and $N = 100$ we find $\tau_p = 1s$. The resulting $50s$ cycle period is short, but not significantly removed from the range available to experiments. The observed mechanism is also consistent with recent experimental work on swelling with selective solvents, where the kinetics of deswelling ordered spheres kinetically favors a vertically oriented cylinder morphology[70].

4.4 Conclusions

We have investigated a new approach to bias the formation of vertically oriented features in block copolymer thin films by cyclic solvent vapor annealing. By averaging time-traces of vertical orientation over statistically independent annealing trajectories, we find strong evidence in support of the hypothesis that the swelling and deswelling processes are critical components that drive reorientation of parallel features. This finding is consistent with experimental observations[4, 55] that significant morphological development occurs during this poorly characterized step in the annealing process. Additionally, the mechanism of order-order transition-mediated orientation in the asymmetric copolymer system suggests an additional handle for tuning performance in these systems. By annealing with a solvent that selectively swells the minority component, the cylinder-sphere transition will be suppressed, extending the stability of perfect cylinders while additionally straining those undermined by nearby defects. In this way, systems with moderate segregation strengths that might normally transition to spheres too early for the CSVA method to be effective may be extended to provide sufficient strain for pattern selection to occur. In aggregate, our results show that repeatedly applying uniaxial strain through swelling with small molecule solvents may be a path towards realizing more robust annealing procedures to

achieve strongly aligned and vertically oriented features in block copolymer thin films.

Chapter 5

Morphology Inverse Design

Modeling and simulation of multiblock polymer (MBP) materials has matured dramatically over the past decade[71–73], and with the advent of powerful hardware accelerators and high performance computing infrastructure, computational methods are playing an increasingly important role in the engineering of these fascinating soft materials[74]. In particular, simulations have been key in exploring the relationship between chain architecture and equilibrium self assembly, paving the way for exciting applications in membrane science[1], energy[10], and lithography for electronic materials manufacturing[75]; all representing opportunities derived from an extended focus on linear AB diblock and ABA triblock polymer phase behavior[76, 77]. While the limited copolymer formulations studied in depth have proven to be broadly useful, they represent only a small subset

of the synthetically accessible molecular design space. Even modest increases in the architectural complexity of MBPs can dramatically expand the range of distinct microphases available[78, 79], potentially enabling unprecedented control over morphology at the nanoscale[8]. Of course, the problem of identifying a molecular design to produce a target nanoscale material morphology is highly non-trivial and a combinatorial approach to searching such a vast design space is entirely impractical. For this reason, it is unlikely that the full potential of MBPs will be realized without the development of new computational tools to aid the design process.

5.1 The inverse design problem

Until recently, theoretical and computational approaches to MBPs have focused on the "forward problem", aimed at predicting equilibrium properties from specified molecular and formulation parameters such as chain architecture, blending ratios, monomer chemistry, and annealing conditions. When designing optimal material formulations, however, the central question runs in the reverse. That is, given a property of interest, such as the size or location of a photonic band gap[80], we seek the formulation specifics of a material that exhibits optimal values of the chosen property. This is not a new concept; it is standard engineering

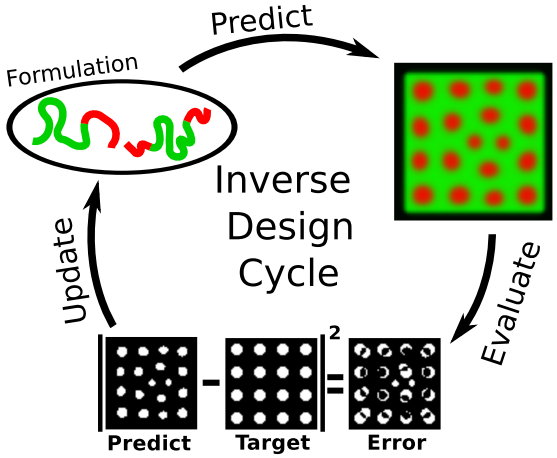

Figure 5.1: Illustration of the inverse design problem treated in this chapter, where a multiblock polymer blend formulation is evolved to reproduce a given pattern through self assembly.

procedure to test material properties and iterate on formulation. The modern challenge is to identify algorithms capable of robustly automating this process, thereby enabling inverse design on problems where manual optimization is untenable or intuition about good designs is lacking. Unfortunately, the infrastructure required for performing automated design of MBP materials has been held back by a few key challenges related to the nature of the optimization problem.

5.1.1 Forward problem definition

In order for the inverse problem to be well-defined, the map from design parameters to predicted properties must be surjective (onto), ie. repeated evaluations of the forward-direction mapping function with the same inputs result in

the same predicted outcome. In this letter, we rely on self-consistent field theory (SCFT) for performing forward predictions, which is able to accurately and efficiently predict structures and free energies of specified mesophases for arbitrary MBP blends[47, 73, 81–83]. In the thermodynamic limit, the equilibrium state of a blend system may be uniquely determined as the lowest free energy solution to the SCFT equations, a sufficient condition for the inverse problem to be well defined. In practice, however, steepest descent relaxation methods, comprising the state of the art in the area, are known to return solutions that depend on the initial field configurations used to seed the calculation, due to a high density of metastable states in the vicinity of the global optimum[8]. This is a significant and outstanding challenge for designing tailored bulk morphologies, and we stress that no comprehensive solution to the issue is supplied here.

Rather, recent work in directed self assembly (DSA) motivates the development of inverse design methods for MBP assembly in reduced dimensionality and laterally confined thin films [51, 84], where we assert that the density of defective states is greatly reduced and the inverse problem becomes well posed. In these applications, a target pattern is specified as a lithographic intermediate to a more complex circuit element, typically composed of isolated line or spot features. The desired features are located on the wafer by etching a confining template for the MBP using standard photolithographic methods. In addition

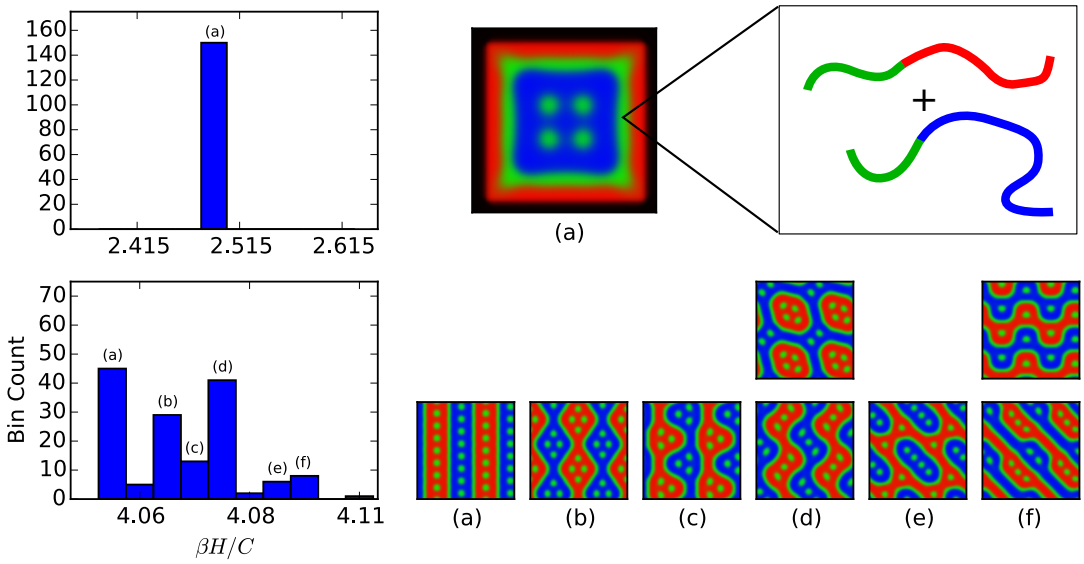

Figure 5.2: Density of states estimates, binned by mean field free energy, for an A-*b*-B + B-*b*-C diblock polymer blend under confinement (top) and periodic boundaries (bottom) relaxed from random initial conditions. Each system contains a symmetric blend of diblock polymers with $\bar{\phi}_{AB} = 0.5$, $f_A^{AB} = 0.7$, $f_B^{BC} = 0.3$, and $\chi_{AB}N = \chi_{AC}N = \chi_{BC}N = 17$. The confined system has equal side wall lengths of $L = 14.5R_g$ with $\chi_{wA}N = -30$ to simulate attractive walls for the A (red) component. Note that two periods (four cells) of the periodic image are shown in the unconfined system to emphasize the bulk morphology.

to smoothing the response surface, restricting our attention to confined systems serves another important purpose. Under thermodynamic conditions that support only a single equilibrium phase, the previous statements regarding the surjectivity of the forward map hold. For bulk systems, however, the possiblity of phase coexistance would need to be accommodated by the forward solution method. Fortunately, in systems under mesoscale confinement, the free energy cost of introducing an interface between coexisting phases is too high to compete for stability

with single phase solutions. We are therefore able to identify the SCFT algorithm as a sufficient method for performing forward predictions. In this context, the inverse design problem reduces to identifying a multiblock polymer formulation whose equilibrium monomer concentration profiles match the target pattern. While others have reported on the inverse problem for pattern selection in this context[85–87], the full design space in those studies consisted of only one or two external template parameters, including the separation distance and selectivity of chemoepitaxial stripes or location of guiding posts, and did not specifically address formulation, nor the challenges of global optimization. Here, we shift the burden of pattern selection to the polymer architecture and attempt to address the global optimization problem underlying formulation design directly.

Before we move on, it is important to clearly state that the density of states reduction relied upon above is difficult to rigorously justify for arbitrary blends. We can, however, gain intuition for when and how strongly this assumption holds by approximating the distribution of states by sampling a large number of SCFT solutions seeded from random initial conditions. The results of this experiment are provided in Figure 5.2, where we compare a blend of two asymmetric diblock polymers relaxed from 150 random initial conditions either under confinement (top) or under periodic boundary conditions (bottom). We bin the results by free energy, where care was taken to ensure that each histogram bin indexes a

single, unique solution to the SCFT equations. In the unconfined system, at least 8 metastable states were identified, where the metastability of each sampled state was ensured by relaxing the residual forces to a strict tolerance of $F_i = \delta\beta H/\delta w_i < 10^{-6}$. In contrast, all simulations of the confined system ultimately settled on the same state regardless of the starting field configuration used. This finding suggests that either the free energy surface for confined systems is strictly convex (the ideal outcome) or that the competing states are kinetically inaccessible to the SCFT relaxation algorithm pseudo-dynamics. We will discuss the implications of this relationship breaking down in subsequent sections.

5.1.2 Blend model and optimization strategy

A second challenge in inverse design relates to the complexity of the fitness metric and its relationship to molecular design parameters. In order to perform global optimization, we require a scalar function of the equilibrium state that measures some distance between predicted and target morphology. Here, we define a metric based on a simple bitmask comparison. As an input to the optimization algorithm, $n_{species}$ binary matrices are provided, corresponding to the desired spatial distribution of the $n_{species}$ distinct monomer types in the system. The pattern

error Ω is determined according to:

$$\Omega = \sum_{\mathbf{r}} \sum_{i=1}^{n_{species}} \left| \rho_i^*(\mathbf{r}) - \widehat{\rho}_i(\mathbf{r};\mathbf{x}) \right|^2, \tag{5.1}$$

where i indexes monomer types, $\rho_i^*(\mathbf{r})$ is the thresholded target monomer distribution, and $\widehat{\rho}_i(\mathbf{r};\mathbf{x})$ is the (thresholded) monomer distribution predicted by SCFT under the conditions described by the design vector $\mathbf{x}$, defined below.

We use self-consistent field theory (SCFT) to predict the self assembly of candidate formulations. The form of the the mean-field Hamiltonian for an arbitrary copolymer blend is a straightforward generalization of the copolymer solution model from the previous chapters[72]:

$$\begin{aligned} \frac{\beta H}{C} =& \frac{1}{2} \int d^3\mathbf{r}' \sum_{jk}^{n_{species}} \chi_{jk} N \phi_j(\mathbf{r}') \phi_k(\mathbf{r}') \\ &+ \frac{\zeta N}{2} \int d^3\mathbf{r}' \left(\sum_j \phi_j(\mathbf{r}') - 1 \right)^2 \\ &- \int d^3\mathbf{r}' \sum_j^{n_{species}} W_j(\mathbf{r}') \phi_j(\mathbf{r}') \\ &- \sum_K^{n_{chains}} \frac{\overline{\phi}_K \tilde{V}}{\alpha_K} \log Q_K[W^K(\mathbf{r}')] \end{aligned} \tag{5.2}$$

where $\beta = 1/k_B T$, $C = \rho_0 R_g^3/N$, N is a reference chain length, $\alpha_K = N_K/N$ is the relative length of chains of type K, $R_g = \sqrt{N/6}b$ is the radius of gyra-

tion for an ideal continuous Gaussian chain, $\mathbf{r}' = \mathbf{r}/R_g$, χ_{jk} are Flory-Huggins interaction parameters, ζN is a harmonic compressibility penalty, and $\tilde{V} = V/R_g^3$ is the normalized cell volume. All concentration fields are normalized so that $\phi_j(\mathbf{r}') = \rho_j(\mathbf{r}')/\rho_0$ is the local volume (blend) fraction of monomers of type j and $\overline{\phi}_K = n_K N \alpha_K/(V\rho_0)$ is the spatially-averaged volume fraction of chains of type K. The fields $W_j(\mathbf{r}')$ are self-consistently determined auxiliary potentials introduced to decouple the multibody interactions in the original particle-based model, and $Q_K\left[W^K(\mathbf{r}')\right]$ is the partition function of a chain of type K. Note that all simulations are performed in two dimensions in laterally confined cells, modelled using the masking method[88, 89] that incorporates a fixed concentration of wall particles $\phi_w(\mathbf{r}')$ into the interaction and compressibility terms of equation (5.2). The pseudo-spectral methods we employ in solving the SCFT equations are well established and we direct the interested reader to the existing literature[21, 28, 72] for details.

In order for the model to be fully specified, we must supply the interaction matrix elements χ_{ij}, the block fractions and architecture of all chains in the system, along with the overall blend composition. While the former poses no challenge, the requirements on valid chain specifications (namely the species block fractions $f_i > 0\ \forall i$ and $\sum_i f_i = 1.0$) render the raw block fractions impractical variables for unconstrained optimization, so a transformation is applied here. For

linear block polymers with n_{blocks} blocks, we may simply define $\beta^K_{i\in\{1,\dots n_{blocks}-1\}} = f^K_i/f^K_{i+1}$ where f^K_i is the fractional length of the ith block of chain K. One then optimizes over the logarithm of these fractional lengths $\gamma^K_i = \log(\beta^K_i)$, so that the chain architecture transitions smoothly between a homopolymer and all possible multiblock polymers, preserving a pre-determined maximum number of blocks, n_{blocks}, and order of block identities, across the range $\gamma \in (-\infty, \infty)$. Computing the associated block fractions f_i from a vector of β values is then a simple matter of solving the linear system:

$$\begin{bmatrix} -1 & \beta_0 & 0 & \cdots & 0 & 0 \\ 0 & -1 & \beta_1 & \cdots & 0 & 0 \\ \vdots & \vdots & \vdots & \ddots & \vdots & \vdots \\ 0 & 0 & 0 & \cdots & -1 & \beta_{n-1} \\ 1 & 1 & 1 & \cdots & 1 & 1 \end{bmatrix} \cdot \begin{bmatrix} f_0 \\ f_1 \\ \vdots \\ f_{n-1} \\ f_n \end{bmatrix} = \begin{bmatrix} 0 \\ 0 \\ \vdots \\ 0 \\ 1 \end{bmatrix}$$

The same approach may be used for the blend composition by defining $\beta^{\bar{\phi}}_K = \overline{\phi}_K/\overline{\phi}_{K+1}$. With these transformations in place, a candidate blend formulation may be characterized by a numerical vector of the following form: $\mathbf{x} = \{\chi_{ij}N \dots, \alpha^K \dots, \beta^K_i \dots, \beta^{\bar{\phi}}_K, \cdots, L_x, L_y\}$. We note that the compressibility parameter ζN is not included in this parameter set, as it is a numerical param-

eter to ensure near incompressibility of the copolymer melt and is held fixed at $\zeta N = 1000$ for all calculations reported here.

5.2 Particle Swarm Optimization

One of the main challenges for the optimization of complex blends resides in the fact that small changes in chain architecture or blend composition may cause features to move suddenly or melt completely from one equilibrium state to the next, precipitating large changes in the pattern error Ω. We may infer from this observation that the function $\Omega(\mathbf{x})$ will exhibit many local optima and therefore poses similar challenges to gradient-based search algorithms as did the original forward problem. This, combined with the high dimensionality of the search space when considering complex blends of MBPs, necessitates the use of a stochastic search algorithm that is both robust to the presence of local minima and able to adaptively balance exploration for promising solutions with exploitation of fit regions to converge to a global optimum.

Particle swarm optimization (PSO) is a powerful global optimization algorithm, historically used more frequently in industrial[90, 91] than academic research, that has been shown to perform well on a broad range of challenging test functions[92]. PSO is a member of a larger group of heuristic algorithms

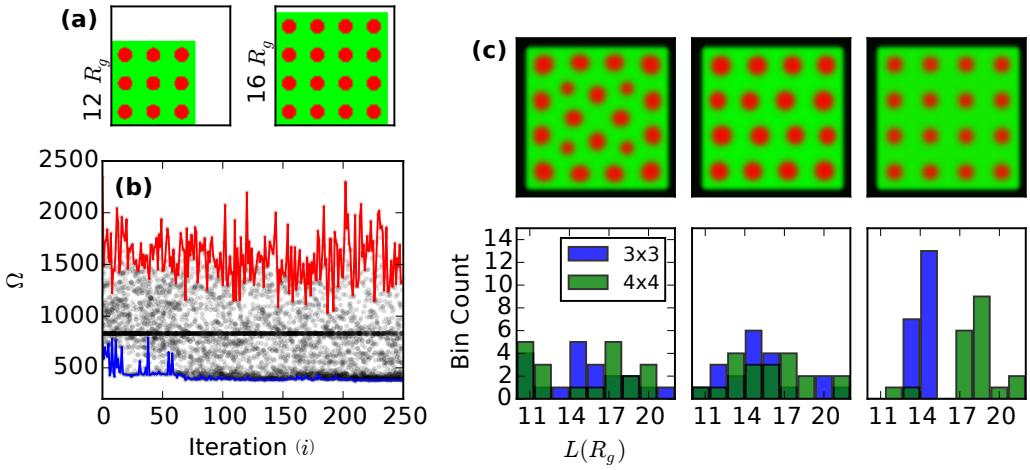

Figure 5.3: (a) Target monomer distributions with minority component (monomer A) packed on an unnatural square lattice in a matrix of monomer B. (b) Scatterplot of the fitness for each agent in the swarm over the PSO trajectory for the 4x4 target. Colored lines trace the most (blue) and least (red) fit agent at each iteration. (c) Histograms of the critical template size parameter L are shown for 3 snapshots of the swarms taken at iteration 1, 30, and 130 from left to right, with the best solution identified at each step shown above.

known collectively as "swarm intelligence" methods[93], unified by the insight that coupling a population of weak optimizers can avoid premature convergence to local optima while efficiently searching a large design space. In the classic PSO algorithm[92, 94, 95], a swarm of agents is initialized with a uniformly distributed set of random positions ($\mathbf{x}_i$) and velocities ($\mathbf{v}_i$) in parameter space and updated

according to the following equations of motion:

$$\begin{aligned}\frac{d\mathbf{v}_i}{dt} =& \chi c_0 \boldsymbol{\xi}(t) \cdot \left(\mathbf{x}_i - \mathbf{x}_i^{pbest}\right) \\ &+ \chi c_1 \boldsymbol{\xi}'(t) \cdot \left(\mathbf{x}_i - \mathbf{x}_i^{nbest}\right) - (1-\chi)\,\mathbf{v}_i \\ \frac{d\mathbf{x}_i}{dt} =& \mathbf{v}_i\end{aligned} \tag{5.3}$$

where $\chi \in (0,1)$ is known as the constriction factor, c_0 and c_1 are positive scalar influence weights, $\boldsymbol{\xi}(t)$ and $\boldsymbol{\xi}'(t)$ are diagonal matrices of random variables uniformly distributed over the interval [0,1), $\mathbf{x}_i^{pbest}$ is the best position visited by agent i in its history, and $\mathbf{x}_i^{nbest}$ is similarly the best position visited by any neighbor of agent i, determined by a communication graph supplied at runtime. While the discrete form of (5.3) is more commonly reported, we write the continuum dynamics here to emphasize the physical process by which the swarm evolves. In this view, the swarm becomes an ensemble of coupled ballistic particles steered towards historically fit states by two elastic force terms, which, combined with inertia and drag, encodes the behavior crossover from exploration to exploitation as consensus grows as to the probable location of the global optimum. Of course, resolving the exact dynamical trajectories is not critical for the heuristic optimization method to perform effectively. Here we adopt the PSO "standard"[92], integrating (5.3) by the Euler-Maruyama method with unit time step ($\Delta t = 1$), setting $\chi = .72984$, $c_0 = c_1 = 2.05$, and implementing a ring neighbor graph so

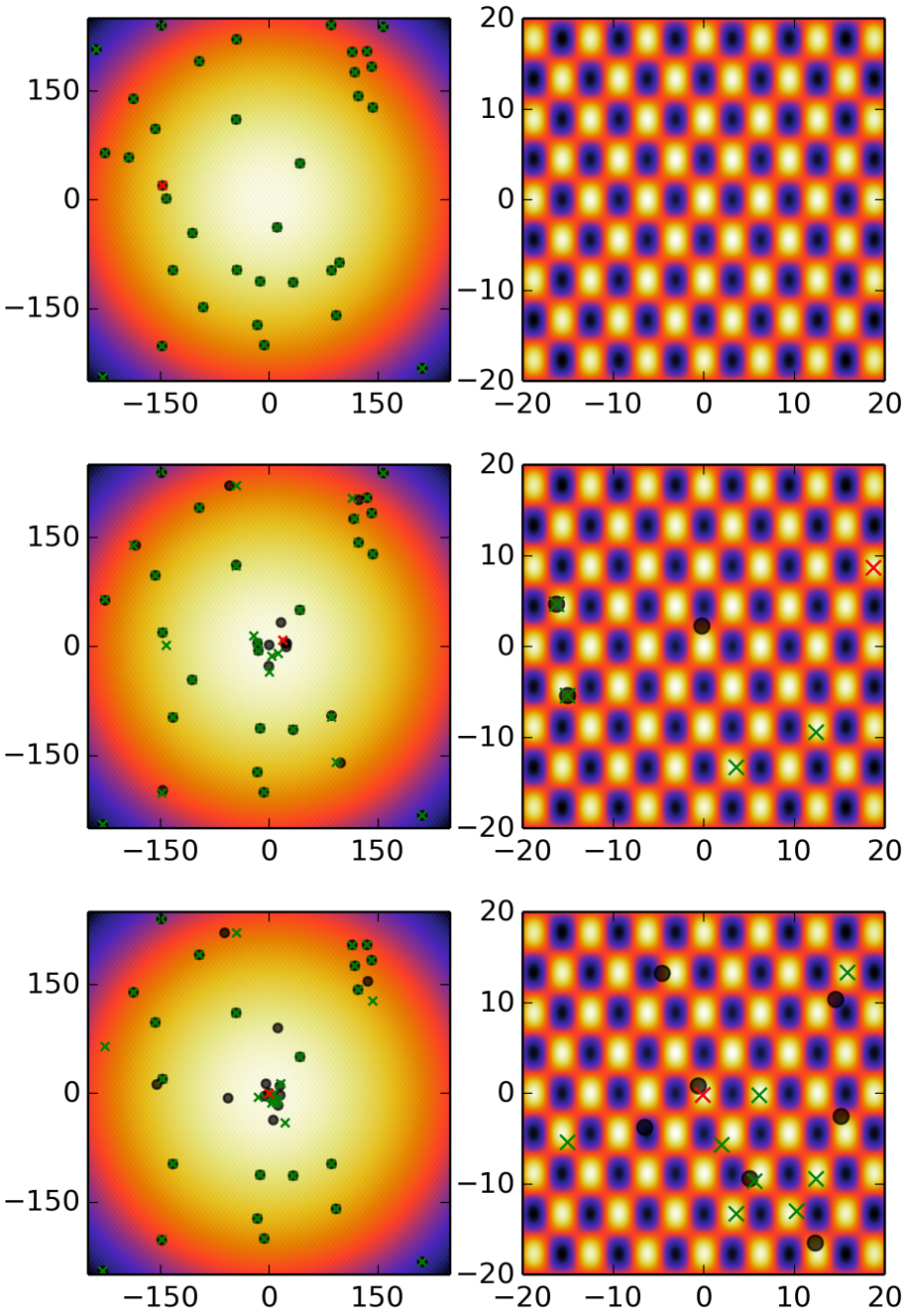

Figure 5.4: Stages of particle swarm optimization on the Griewank test function. Snapshots are taken at iteration 0, 36, and 72 (top to bottom). In each row, the right column is merely an amplified view of the region surrounding the global optimum at $(x_0, x_1) = (0, 0)$. Green crosses indicate a *local* best position of an agent in the swarm, while the red cross indicates the *global* best position identified so far.

that each agent a_i has two neighbors: a_{i-1} and a_{i+1}, with periodic boundaries at the end nodes.

The PSO algorithm is simultaneously intuitive and opaque in its behavioral approach to optimization. In order to facilitate a basic understanding of the hierarchical search performed by the swarm during a PSO simulation, we have illustrated a swarm trajectory using the Griewank test function as the fitness metric (Figure 5.4):

$$f(\mathbf{x}) = \sum_{i=0}^{1} \frac{x_i^2}{4000} - \prod_{i=0}^{1} \cos\left(\frac{x_i}{\sqrt{i}}\right) + 1 \tag{5.4}$$

In the begining of the simulation, the uniformly distributed agent positions set the initial $\mathbf{x_i^{pbest}}$ and $\mathbf{x_i^{lbest}}$ across the entire domain. By iteration 36, however, we can clearly see the distribution of $\mathbf{x_i^{pbest}}$ and $\mathbf{x_i^{lbest}}$ positions to become peaked near the global optimum at $(0, 0)$. As consensus grows, the velocity of the particles near the center drops due to the drag term in the equation of motion and a local search finally spots the global optimum by iteration 72. It is impressive that a stochastic search method with no direct gradient terms could so quickly identify such a localized optimum across so few iterations.

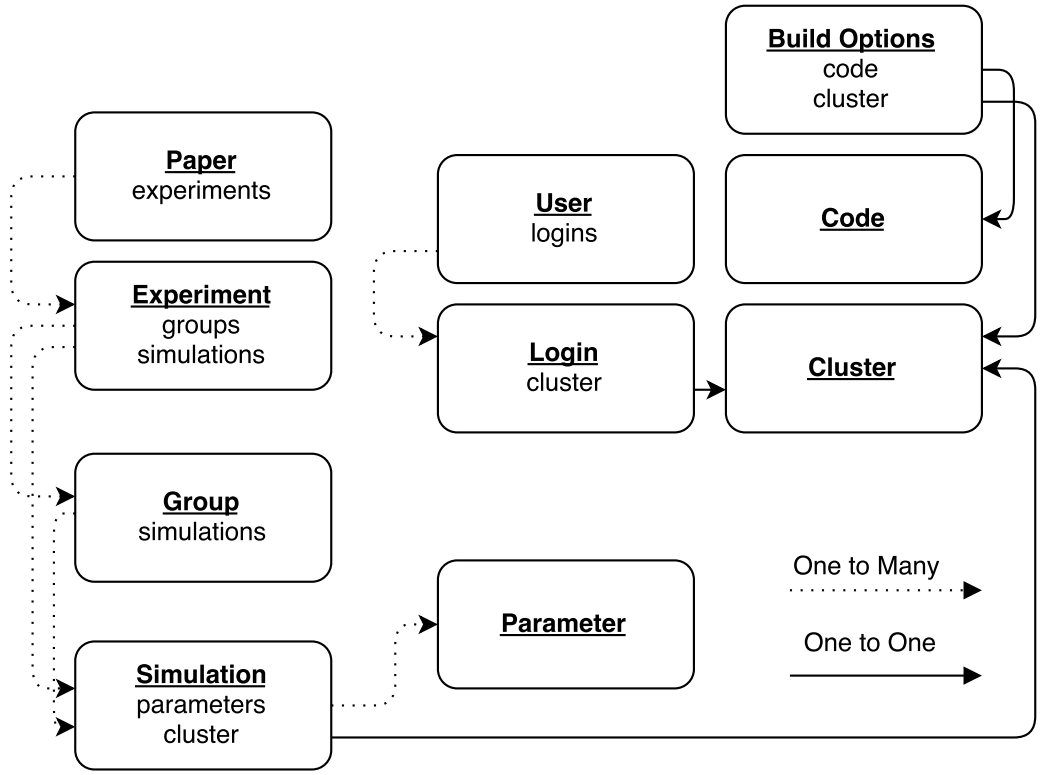

Figure 5.5: The relational database schema underlying the Experiment Organizer package. Arrows indicate record relationships between tables.

5.2.1 A note on infrastructure and implementation

While the particle swarm optimization update scheme in (5.3) is quite straightforward to implement, the evaluation of the fitness function requires that one or more self-consistent field theory calculations be performed, observed, and have their results analyzed before the particle positions are updated and the algorithm continues. For a swarm of size $n = 30$ run for 250 iterations, a minimum total of 7500 field theory calculations will be run. When this number of interacting

calculations are run through an automated system, error handling and detection is critically important both for ensuring integrity of the data propagating through the system as well as ensuring that the calculation runs smoothly to completion in the face of possible unplanned outages or queue failures. Much of this infrastructure is bundled into a library called the **Experiment Organizer**, although there are tentative plans to refactor it into a new project with a pithier monicker (**Jeeves**). The **Experiment Organizer** is broken into three major components: a **Parameter Factory** to produce parameter files for new simulations, an ORM (object relational map) wrapper and associated MySQL database (defined in **table_def**), and a driver (**FTS_DB**) that draws on the other pieces to assemble and execute calculation pipelines.

Arguably the central organizing element of the framework is the database, whose (heavily coarse-grained) schema is outlined in 5.5. As the purpose of the software is to provide an abstraction layer around the execution of a single simulation, the **Simulation** table may be considered the core element of the database. The ORM enables SQL tables to be represented as Classes whose instances represent rows in the database. With a **Simulation** record instance, all relevant information regarding the runtime, fate, and physical parameters used in the calculation it represents is immediately available either directly through the instance variables (mapped from columns in the table through the ORM) or through the

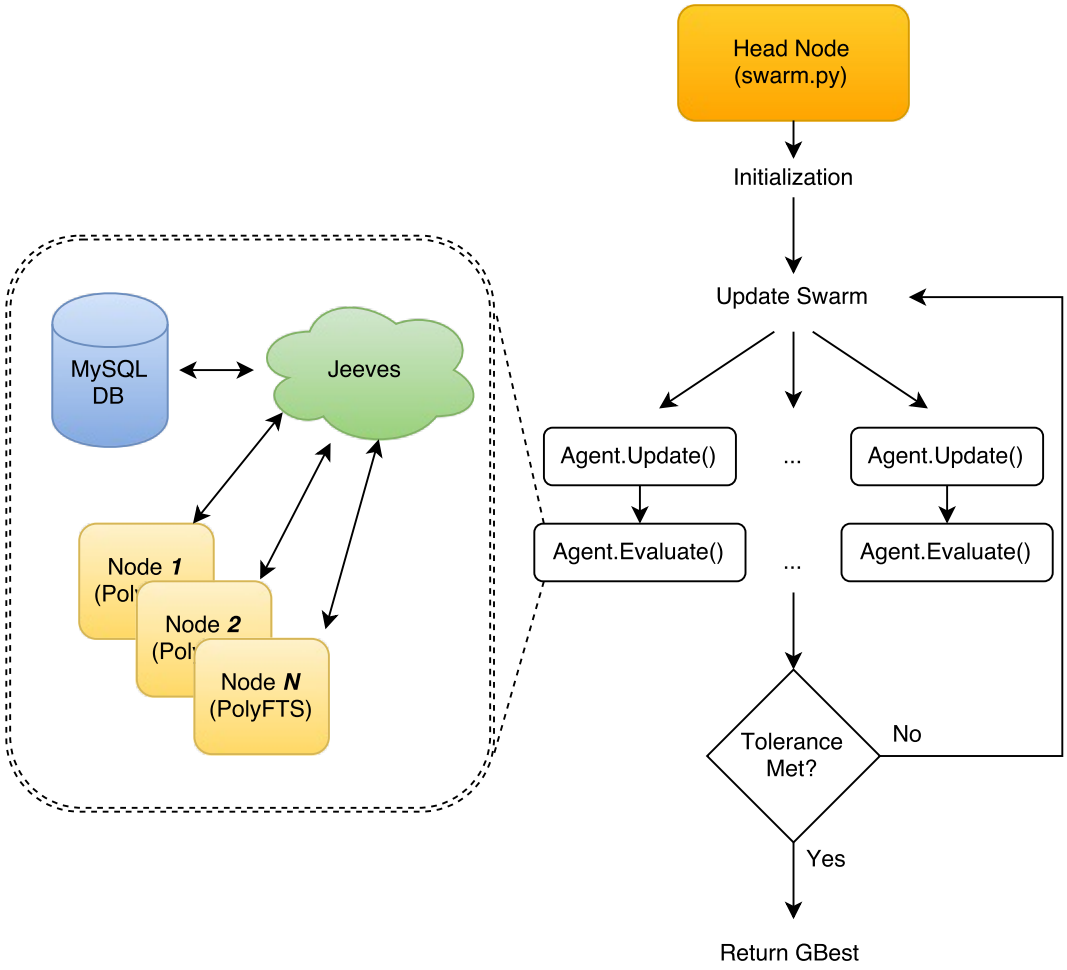

Figure 5.6: The basic flow of logic through the particle swarm optimization routine. The simulation runs on a single head node, which instantializes a *Swarm* and array of *Agent* objects. Every step, the swarm iterates over each agent and updates its position and velocity vectors according to the PSO algorithm. Once updated, each agent re-evaluates their fitness by running the required Self-Consistent Field Theory calculations via a series of requests to the Jeeves library (formerly Experiment Organizer).

FTS_DB library. The following is a minimal working example demonstrating basic usage and interaction with a **Simulation** record:

```
import FTS_DB as FTS
from table_def import Simulation

# Start a database transaction
s = FTS.Session()

# Pull a random simulation record from the database
sim_record = s.query(Simulation).filter_by(id=173245).one()

# Assuming this record represents a PolyFTS simulation, we
# can parse the Hamiltonian associated with the final,
# converged state from `operators.dat`:
# The following locates the physical location of the simulation,
# be it a remote cluster or local disk, and searches for a file
# matching 'operators.dat'. If found, the file is downloaded to a
# local cache and the filepath is subsequently returned.
local_fname = FTS.GrabFile(sim_record, "operators.dat")
with open(local_fname, 'r') as f:
    last_line = f.readlines()[-1]

    # The first two columns in operators.dat are the iteration
    # number and value of the Hamiltonian
    time_step, hamiltonian = last_line.split()[0:2]

# Simulation parameters can be accessed
# and set using a fuzzy getter/setter pattern:
sim_record.get("DT")
# exact matches return the value
# fuzzy matches return a dict (hash table): {"TimeStepDT": 0.1}

# We can also set parameter values
# If FTS.RerunSimulation() is called after Simulation.set(), the
# new TimeStepDT parameter value will be used in the calculation:
sim_record.set(TimeStepDT=0.2)
FTS.RerunSimulation(sim_record)
```

This example covers a very small fraction of the overall functionality but is sufficient to demonstrate the essential methods for manipulating and retriev-

ing data from the **Simulation** record. The balance of the database is devoted to storing information required to enable the automated compilation and deployment of simulation codes to the clusters available on campus and on the national supercomputing network. For further detail on implementation and usage, the interested reader is directed to the documentation hosted on the Gitlab server (*polybot.mrl.ucsb.edu* at time of writing). In particular, the **SimulationLauncher** class is the primary workhorse of the particle swarm codes and should be understood before attempting to extend any functionality.

With this background in place, we can progress to discussing the implementation of the particle swarm optimization routines and opportunities for its extension. The flow of control flow in the particle swarm optimization algorithm is illustrated in Figure 5.6. All codes begin by determining the network topology of the swarm and the flavor of the Agents that will populate it. Once agents are instantialized, the **Update** method of each is called, which offers the first entrypoint for customizing the behavior of the swarm. The **Update** method in the **Agent** class implements the "standard" algorithm[92] which may be modified one of two ways. First, in the most extreme case, the **Update** method may be overloaded entirely by subclassing **Agent**, defining a matching method signature, and implementing the new algorithm there. If this route is taken, a call to **self.Evaluate()** must end the method block in order for the fitness to be

recalculated and the program to continue properly. There are many variants of the particle swarm method, however, that rely on more subtle modifications such as the inclusion of a dynamically updated constriction factor[96] ($\chi(t)$) or additional body forces[97]. These may be incorporated by writing a lightweight mixin class. The following illustrates the mixin method for incorporating an additional repulsive body force according to the Charged Particle Swarm Optimization[97] method:

```
from Sean.Swarm import Agent, SCFTAgent

# The charged agent generates a Coulomb body force
class ChargedAgent(Agent):
    def __init__(self, charge, **kwargs):
        self.q = charge
        super(ChargedAgent, self).__init__(**kwargs)

    def Update(self):
        # TODO: Compute Coulomb forces
        a = np.zeros(self.Location.ScaledCoords())
        for agent in self.parent_swarm:
            a += coulomb(self, agent)
        super(ChargedAgent, self).Update(acceleration=a)

# Customized Agent to be added to the Swarm
class MyAgent(ChargedAgent, SCFTAgent):
    def __init__(self, **kwargs):
        super(MyAgent, self).__init__(**kwargs)

    # Overload ComputeFitness to define the fitness function
    def ComputeFitness(self):
        # TODO: define fitness function
        pass
```

After the **Update()** method is run, **Evaluate()** is executed to compute the fitness function of the new set of candidate solutions. For the morphology optimization calculations discussed in this chapter, a single self-consistent field theory calculation is run. A number of opportunities for tuning the fitness function to more reliably return robust and physically meaningful solutions are discussed in later sections. Each of these, including averaging the results of multiple independent runs, e.g., would be implemented by overloading the **ComputeFitness** method in a custom subclass of **SCFTAgent**.

5.2.2 Application to DSA targets

We now turn our attention to examples illustrating the application of the PSO method for blend optimization. One of the more promising applications for BCP lithography in semiconductor manufacturing is in patterning VIA (vertical interconnect access) arrays[98]. Recent efforts in this area have focused on the "hole-shrink" problem, where an asymmetric diblock polymer melt with an etchable minority block is annealed under cylindrical confinement resulting in a 1:1 correspondence between photolithographically patterned cylindrical templates and narrower self-assembled VIA cylinders representative of the minority block domain. In an attempt to simplify the process and improve feature density, one may seek a diblock formulation that has been tailored to self assemble directly into

a full VIA array with proper registry if deposited into a larger (non-cylindrical) template. This problem has been studied previously for a square 16-cylinder template[89] and a solution is known to exist with large molecular weight homopolymer additive blended in small amounts with asymmetric diblock chains. For a PSO demonstration, we fix $\chi_{AB}N = 17$ and optimize formulation parameters for a two-chain system where $\mathbf{x} = \left\{\alpha_{AB}, \alpha_{Bh}, \beta^{AB}, \beta^{\bar{\phi}}, L\right\}$. Limiting ranges were imposed on the search space corresponding to diblock fraction $f_A \in [0.1, 0.5]$, blend composition $\overline{\phi}_{AB} \in [0.7, 1.0]$, template size $L \in [10, 20]$, and chain lengths $\alpha \in [0.5, 2.0]$. Note that in this and all subsequent demonstrations, we use a swarm with $n_{agents} = 20$. The confining well used in each SCFT simulation was constrained to be square for simplicity, with $L_x = L_y = L$, and with walls that are selective to the matrix component (B), $\chi_{wB}N = -30$.

The results of the optimization are shown in Figure 5.3. The window of stability for square-packing is known to be quite wide along the homopolymer additive length and diblock fraction[89] parameters, and the relative ease of the optimization problem is reflected in the rapid identification of a high-quality solution after only 60 iterations. One key measure of the robustness of a global optimization strategy is in its ability to maintain population diversity after identifying quality solutions, as the global optimum is rarely known *a priori* and a better solution may exist. It is therefore encouraging to note that, despite having settled on an

excellent solution early in the trajectory, the swarm remains diverse after more than 250 iterations (Figure 5.3b). This does not mean that no evolution of the swarm structure has occurred during this time. Indeed, looking at the distribution of L (Figure 5.3c) across the swarms for both small 9-cylinder and larger 16-cylinder templates, we see each quickly learns that the best solutions are unambiguously located around $L = 13R_g$ and $L = 18R_g$ respectively. This observation highlights one of the key mechanisms of the PSO technique. While the agents' inertia maintains diversity in parameters that continue to change as new fit solutions are identified, any parameters that directly correlate with the fitness of solutions will converge independently at a rate determined by the drag coefficient $(1 - \chi)$. This consensus mechanism allows the swarm to efficiently search high-dimensional spaces by systematically removing parameters from consideration as their direct correlation with the fitness function becomes clear.

With this background in place, we shift our focus to more challenging design features to demonstrate the feasibility of formulation optimization within the PSO framework. Our targets are motivated by one of the modern challenges in DSA for semiconductor patterning: stabilizing complex patterns with coexisting, heterogeneous features[99]. We begin with an extension of the square packing example, where all spots except those at the four corners are removed and a single extended line feature is inserted in place of the middle row (Fig-

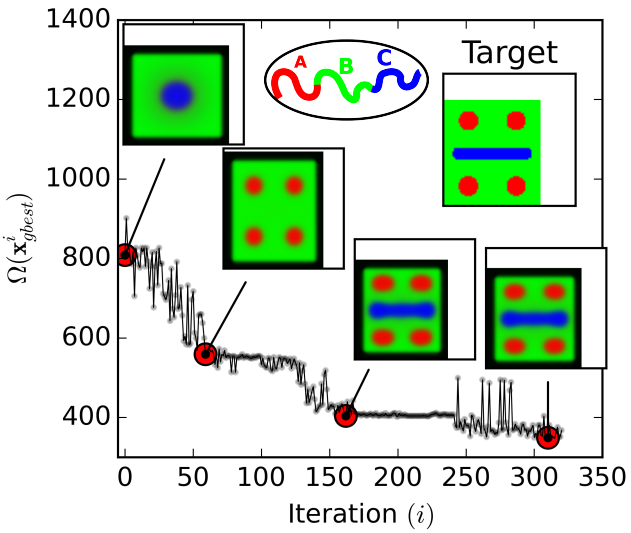

Figure 5.7: Convergence of a multiblock blend formulation designed to stabilize coexisting line and spot features. The fitness of the *best agent* in the swarm ($\mathbf{x}^i_{gbest}$) is plotted for each iteration with four solutions highlighted (red circles) to illustrate evolutionary milestones. The target pattern is displayed in the upper right inset.

ure 5.7). In order to provide sufficient flexibility for the algorithm to identify a quality solution, three chains were included in the initial formulation: one B homopolymer and two ABC triblock chains. The interaction parameters between monomers were again fixed with $\chi_{AB}N = \chi_{AC}N = \chi_{BC}N = 18$ and wall interactions set to be strongly selective for the B monomer (green) with $\chi_{wB}N = -30$. While interaction parameters were witheld from the search space, we stress that this does not imply that such added flexibility would ruin optimization performance. We expect that added model flexibility will be crucial for identifying solutions to many interesting patterns and that this is a profitable direction for

future work. The remaining parameters for optimization form the design vector $\mathbf{x} = \left\{\alpha_h, \alpha_{t0}, \alpha_{t1}, \beta_0^{t0}, \beta_1^{t0}, \beta_0^{t1}, \beta_1^{t1}, \beta_0^{\overline{\phi}}, \beta_1^{\overline{\phi}}, L_x, L_y\right\}$ where $t0$ and $t1$ denote the parameters associated with the two triblocks and h the homopolymer chain. In order to accelerate the search, reasonable constraints were applied to the template size and relative chain length parameters so that $L_x \in [11, 14]$, $L_y \in [12, 16]$, $\alpha_{t0}, \alpha_{t1} \in [0.9, 1.3]$, and $\alpha_{Bh} \in [0.5, 2.0]$. Importantly, the parameters associated with the triblock architectures $(\beta_{0,1}^{t0}, \beta_{0,1}^{t1})$ were practically unconstrained, with $\gamma \in [-4, 4]$.

The evolution of candidate solutions over the optimization trajectory is shown in Figure 5.7, illustrating the hierarchical search that is characteristic of the PSO method and related evolutionary algorithms. At early times, relatively poor solutions are identified and continuously improved until the first major morphological milestone is accomplished, with the outer four spot features in place. The solution quality then stagnates, maintaining diversity in most parameters while beginning to converge the features that consistently result in quality solutions (such as the inclusion of an asymmetric AB diblock chain type, responsible for the corner spots) until an agent eventually incorporates a symmetric BC chain into the blend, resulting in the first qualitatively correct solution with a C-rich domain extending through the center of the cell. Further optimization results in subtle improvements in pattern error, such as shortening chains to slim the spot

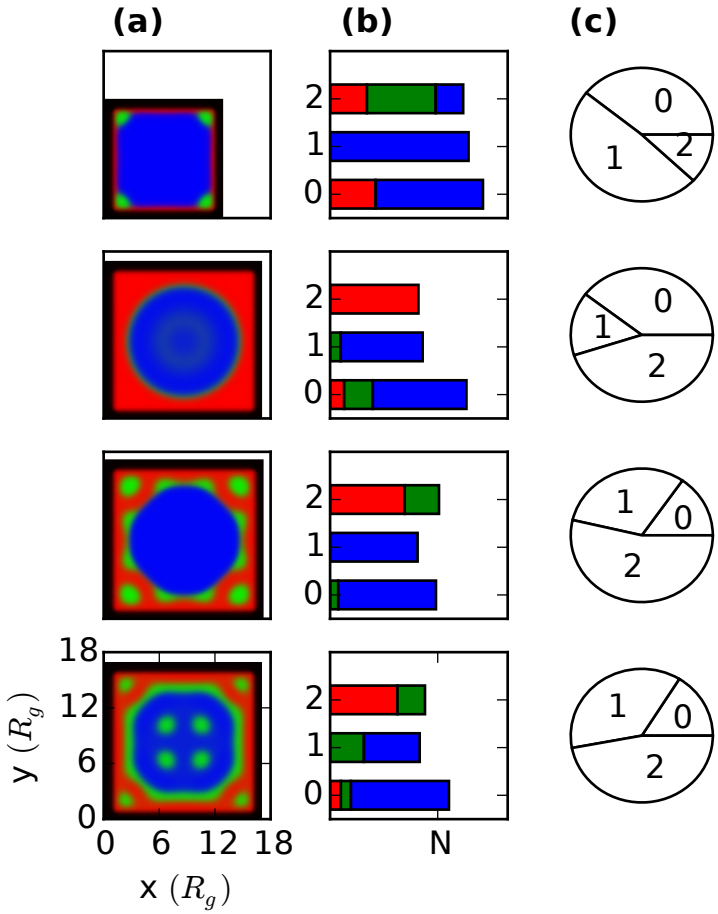

Figure 5.8: PSO simulation results featuring a completely unconstrained blend of three *ABC* triblock chains. The target pattern, not shown, is essentially identical to the final solution (lower left). (a) Evolution of the equilibrium structures (iteration number increases top to bottom). (b) Chain architecture schematics with block fractions indicated by the length of colored segments, and normalized molecular weight by total bar length. (c) Overall blend composition (index labels correspond to chain indices in (b)).

features and adjusting the confining mask dimensions to correct placement error.

It is interesting to note that, by the end of the optimization trajectory, the original triblock chains have been nearly reduced to diblocks with $f_A^{t0} = .08$, $f_B^{t0} = .46$,

$f_C^{t0} = .46$ for the first chain and $f_A^{t1} = .36$, $f_B^{t1} = .64$, $f_C^{t1} = .00$, for the second with an overall blend composition of $\overline{\phi}_{t0} = 0.31$, $\overline{\phi}_{t1} = 0.49$, and $\overline{\phi}_h = 0.20$.

As a final test, we generated an ensemble of morphologies from SCFT simulations launched from random seeds covering a range of diblock polymer blends in order to identify a challenging pattern for the algorithm to reproduce. The target was chosen from a blend of asymmetric AB and BC diblock chains with no additive. In order to further test the algorithm's ability to efficiently eliminate unnecessary chain degrees of freedom during optimization, no information was passed on to the PSO algorithm in the form of block fraction or blend limitations, except that the final solution must be derived from a blend of 3 ABC triblock polymers. In practice, one will not necessarily know *a priori* what degree of architectural complexity will be necessary to generate a desired template. Figure 5.8 highlights four states along the optimization trajectory that follows the same systematic evolution procedure as demonstrated previously, adding and refining features to converge consistently more fit solutions as the swarm evolves. These results illustrate the wide range of formulations sampled during optimization, from an ABC + C + AC blend with a majority homopolymer (top row Figure 5.8b) to an A + highly asymmetric BC + highly asymmetric ABC triblock, then ultimately the known solution with an AB + BC + C blend. Although the homopolymer ad-

ditive is known to be superfluous, it doesn't appear to negatively impact pattern fidelity.

5.2.3 Fitness engineering for robust solutions

In earlier sections, we stressed that the reduction in the density of solutions under confinement is not a rigorous feature of the field theory, simply an empirical observation that has held through our investigation. As formulations become more complex, the density of defective states may increase, leading to the possibility that a solution identified by the PSO method will be either kinetically inaccessible or, worse, only metastable. Unfortunately, little can be done in the case of the former without augmenting the theory with dynamical information. Still, the Nudged Elastic Band or String method[100], recently adapted for polymer field theory models[101], may be used to, at minimum, ensure that a kinetic path from disorder to the candidate state exists. Modifying the fitness fuction so that these solutions are less likely to be selected during the optimizing process, however, would likely prove too computationally expensive to be viable.

The concern regarding metastability of converged solutions is much easier to address as it is fundamentally an issue of sampling the distribution of locally stable states at equilibrium. To do this rigorously would require exhaustively enumerating the field degrees of freedom and, as discussed in previous sections,

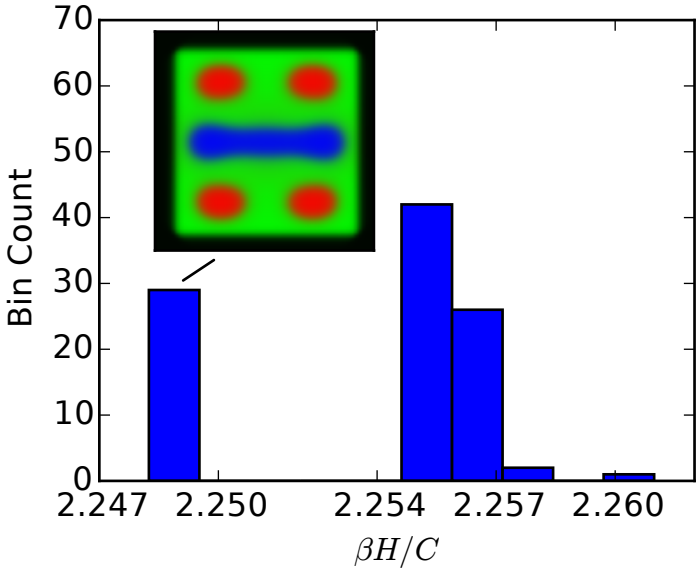

Figure 5.9: Density of states estimate for the final PSO solution reported in the main text. Each calculation was a blend of two A-*b*-B-*b*-C triblock polymers and B homopolymer annealed under confinement. Parameters for each of the 100 random quenches were: $L_x = 11.9R_g$, $L_y = 12.5R_g$, $\mathbf{f}^{t0} = \{.08, .46, .46\}$, $\mathbf{f}^{t1} = \{.36, .64, 0.0\}$, $\alpha_{t0} = 0.93$, $\alpha_{t1} = 1.0$, $\alpha_h = 0.95$, $\phi_{t0} = 0.31$, $\phi_{t1} = 0.49$, $\phi_h = 0.20$ where $t0$ and $t1$ index the triblock chains and h indicates the homopolymer.

an efficient solution to the forward problem is the focus of active research. While a global solution to the forward problem is not yet available, we may still gain valuable insight into the competing metastable states by sampling solutions to the SCFT equations. As an illustration of this approach, the solution we obtained from running PSO on the triblock blend system (Figure 5.7) aimed at stabilizing the mixed feature pattern was tested for stability by running 100 random quenches at the conditions identified by the optimizer. Figure 5.9 shows the results of these calculations, binned by the mean-field free energy of each stationary solution. It

is satisfying to see that the state with the lowest free energy, which is therefore expected to be the most probable state at equilibrium, does in fact correspond to the target morphology. In this sense, the PSO algorithm performed as expected. However, it is clear from the significant population of non-target states in the histogram that the influence of confinement was insufficient to destabilize all competing solutions. While the algorithm was successful in returning a valid solution, the result is fortuitous in the sense that a different random seed may have caused the agent responsible for the solution here to have converged a competing metastable state.

This issue may be avoided by engineering the fitness metric to bias the algorithm towards more robust solutions during the optimization process. This approach, if effective, is clearly preferred over filtering candidates identified after the optimization routine completes as the calculations can take over a week to complete. In the current algorithm, the fitness of a candidate solution is determined by running a single self-consistent field theory calculation and simple image analysis on the resulting morphology. One straightforward modification would be to run two calculations during the agent fitness evaluation step: one from a random field configuration and the other seeded with the target morphology. The solution with the lower free energy can then be chosen as the stable solution and the morphology analysis done using results from that simulation. In

this way, candidate blends for which the target pattern is the most stable state but where the field relaxation kinetics artificially prefer a competing state would correctly choose the seeded simulation as the appropriate one to use in the fitness calculation. Similarly, if the target pattern does not correspond to the lowest free energy state but erroneously converges to it from a random field configuration, then this method will appropriately filter this result as well. This alternative evaluation method is attractive for a number of reasons. First, it explicitly safeguards against the two primary failure mechanisms identified above. In addition, the computational burden is only increased by a factor of two, while alternatives that involve sampling the density of states as we have done above to test the final solution can quickly become prohibitively expensive.

5.3 Conclusions

In this chapter, we have described and demonstrated the effectiveness of a global optimization strategy for identifying multiblock polymer blends that self assemble into nontrivial target patterns. Despite the large degree of architectural flexibility provided to the algorithm, we find that the hierarchical search executed by the PSO dynamics is well suited to finding quality candidates in a sparse solution space, and, in instances where greater architectural flexibility was provided

than is known to be necessary, the algorithm efficiently digests the unnecessary degrees of freedom to return the expected solution. These results demonstrate that the PSO algorithm is capable of inverting the relationship between morphology and chain architecture. We hasten to note, however, that while the success of the PSO algorithm can be linked to its unique approach to optimization, there is every reason to suspect that similar evolutionary algorithms, such as the popular CMA-ES[102, 103], could be similarly effective. Now that the viability of this approach to the inverse problem has been demonstrated, a number of fruitful future directions can be envisioned. While still considered the modern standard, the PSO algorithm used here neglects nearly a decade of improvements published in the literature, including adaptive variants[96, 104] that dynamically adjust the agents' drag coefficients in order to more intelligently manage the transition from exploration to exploitation in search of global optima, the inclusion of which may meaningfully improve performance in more demanding applications. In addition, further engineering of the fitness function to include penalties for chain or blend complexity or solution robustness may improve the likelihood of identifying solutions that are practical to realize commercially as well as exhibiting optimal response properties.

Finally, optimizing polymer materials based on properties other than morphology is an exciting prospect with no obvious barrier based on the present work.

One may imagine, for instance, replacing the pattern error fitness metric with a measure of the interfacial area between distinct monomer types and a penalty for non-percolating domains of another (e.g., measured via a burning algorithm) to generate bi- or tri-continuous candidate materials for high-performance organic photovoltaics or advanced membranes. In such applications, numerous constraints on chain types, monomer chemistry, pure block physical properties, and material morphology conspire to make manual design exceptionally challenging. Finally, while the blend representation used in the present work is limited to linear chains, extensions to handle more complex architectures (e.g., continuously evolving the location and density of branch points in a comb polymer) would enable researchers to fully exploit the molecular design flexibility of MBPs.

Chapter 6

Conclusions and opportunities for future work

As a collection, the chapters of this thesis have attempted to make modest steps in furthering our ability to devise and engineer new nanostructured materials from block copolymers. This effort was distributed across two primary goals; the first aimed at understanding morphology dynamics during solvent processing and the second focused on the inverse design problem of identifying block copolymer blends that satisfy a set of pre-determined design constraints.

In order to address problems associated with solution processing, an investment in some new methods was first required. No single piece described in chapter 2 was revolutionary; rather the need to build a consistent framework capable of

efficiently capturing diffuse solvent gradients and slow interdiffusion processes while resolving thin layers of active material required a number of small enhancements to be built and assembled. We have described an efficient method for allowing solvent evaporation to occur, a fundamentally nonequilibrium process, while computing the chemical potential fields driving monomer motion based on a quasi-equilibrium assumption. In addition, aspects related to ensuring that the boundary conditions applied at all levels of the model hierarchy were consistent and strategies for ensuring that the conservation of polymer segments was preserved were discussed.

With efficient methods for simulating a drying film established, we began with the problem of evaporation-induced self assembly. Ever since the seminal publication in the late 90s by Kim and Libera[7], the idea of driving microphase separation by rapid evaporation has tantalized materials scientists trying to make nanostructured films that utilize highly ordered and vertically oriented features. Since those early results, a number of promising[1, 2, 5] and challenging[6] reports have been made regarding the efficacy of the approach. In chapter 3, we highlight the difficulty in stabilizing ordering fronts with vertically oriented features despite ostensibly ideal conditions of perfectly neutral solvent and free surface interactions. As a result, we were motivated to study the growth of ordered phases into disordered fluid and found that this process was significantly more stable for

lamellae and cylinders oriented parallel to the plane of the free surface than those oriented perpendicular. By studying the correlation of fluctuations at the interface of the ordered and disordered fluid on either side of a steady-state ordering front, we were able to connect this reduced stability to the block copolymer chain architecture. This insight is very promising, as it provides a potential avenue for rationally devising copolymer systems that are most likely to generate stable ordering fronts with the desired orientation. Looking forward to opportunities for future work, it would be intriguing to see if other, more complex phases could be templated by a careful selection of polymer architecture that was able to enhance correlations at the ordering front that are consistent with the propagation of a desired microphase. At a minimum, it would be interesting to see if our prediction that a triblock system whose minority component comprised the *midblock* of the chain would generate more stable vertically oriented cylinder fronts than diblock polymers or the inverted triblock.

In chapter 4, we attempted to strafe the issue of evaporation-induced ordering and suggest a viable alternative that relies on the strain that film swelling during solvent uptake imparts on the film's internal morphology to drive the desired orientation. We find that this approach enjoys much broader operating windows for achieving well-ordered and uniformly oriented domains than rapid solvent evaporation alone and demonstrate that the same principles apply to both

lamella and cylinder-forming systems. Furthermore, we showed that the results were insensitive to the rate of solvent uptake/evaporation. This study provides sufficient motivation, in our view, to test the predictions made in an experimental system. Two key assumptions were made in this study, however, that should be considered further before moving forward. The first is the assumption of neutral (non-preferential) interactions between the copolymer blocks and the free surface and substrate. While there are experimental techniques for achieving these conditions, such as placing films on random copolymer mats[105] and tuning the composition of solvent atmosphere to be effectively neutral, due diligence must be done to ensure that the results are not highly sensitive to neutrality conditions. The second significant assumption was that the films can be cycled quickly enough so that the relatively slow process of terracing (island and hole formation) does not occur. These structures come at significant cost in free energy, associated with the additional interface exposed to the atmosphere, however, so it is unlikely that they will persist through multiple cycles, but the eventuality should be accounted for.

Having closed our conversation on solvent annealing methods, we take a step back in chapter 5 to consider a problem of significant contemporary interest - that of inverse design. By adapting the particle swarm optimization method for use with polymer field theory calculations, we were able to demonstrate the direct and

largely unguided inversion of morphology to formulation parameters. This is the first successful attempt, to the best of our knowledge, to apply global optimization strategies to the identification of block copolymer architectures that exhibit desirable properties in the melt state. While not without significant challenges, most notably the lack of a rigorous forward mapping procedure in the general case, this work appears to rest on fertile soil for future developement. Clearly, the exclusive focus on linear block copolymers that was taken in the examples here is not a necessary restriction. A much more rich architectural landscape will be accessible when the vectorized description of the chain architecture is generalized to include branching. This is an exceptionally exciting area as the number of degrees of freedom make systematic exploration onerous, although it is likely that carefully chosen branches may be crucial ingredients to stabilizing traditionally challenging morphologies such as double diamond or single gyroid, predicted to have unique optical properties[106, 107]. Once this degree of flexibility is available, formulations that stabilize these exotic phases may be identified by maximizing the difference in free energy between the preferred microphase and the next lowest free energy structure. The challenges related to the forward problem in the bulk can be mitigated by simply establishing a list of candidate structures to check at each point in formulation space. It is clear that many opportunities exist to build on the work presented here.

In conclusion, our work has elucidated some important features of evaporation-induced ordering and solvent annealing in inhomogeneous polymer systems and has introduced a powerful global optimization strategy to search for "designer" polymer formulations in an automated fashion. As the field continues to demand more flexibility in design and requirements on performance, automated methods for searching the vast whitespace of block copolymer formulation will only increase in relevance. It is our hope and belief that the methods developed here will aid in furthering that effort.

Bibliography

[1] Jackson, E. A.; Hillmyer, M. A. *ACS Nano* **2010**, *4*, 3548–3553.

[2] Phillip, W. A.; O'Neill, B.; Rodwogin, M.; Hillmyer, M. A.; Cussler, E. L. *ACS Applied Materials & Interfaces* **2010**, *2*, 847–853.

[3] Ulbricht, M. *Polymer* **2006**, *47*, 2217–2262.

[4] Sinturel, C.; Vayer, M.; Morris, M.; Hillmyer, M. A. *Macromolecules* **2013**, *46*, 5399–5415.

[5] Kim, S. H.; Misner, M. J.; Xu, T.; Kimura, M.; Russell, T. P. *Advanced Materials* **2004**, *16*, 226–231.

[6] Albert, J. N. L.; Young, W.-S.; Lewis, R. L.; Bogart, T. D.; Smith, J. R.; Epps, T. H. *ACS Nano* **2012**, *6*, 459–466.

[7] Kim, G.; Libera, M. *Macromolecules* **1998**, *31*, 2569–2577.

[8] Bates, F. S.; Hillmyer, M. A.; Lodge, T. P.; Bates, C. M.; Delaney, K. T.; Fredrickson, G. H. *Science* **2012**, *336*, 434–440.

[9] Mistark, P. A.; Park, S.; Yalcin, S. E.; Lee, D. H.; Yavuzcetin, O.; Tuominen, M. T.; Russell, T. P.; Achermann, M. *ACS Nano* **2009**, *3*, 3987–3992.

[10] Darling, S. B. *Energy & Environmental Science* **2009**, *2*, 1266.

[11] Hamley, I. W. *Nanotechnology* **2003**, *14*, R39–R54.

[12] Paik, M. Y.; Bosworth, J. K.; Smilges, D.-m.; Schwartz, E. L.; Andre, X.; Ober, C. K. *Macromolecules* **2010**, *43*, 4253–4260.

[13] Doi, M.; Edwards, S. F. In *The Theory of Polymer Dynamics*, 1st ed.; Birman, J., Edwards, S. F., Llewellyn Smith, C. H., Rees, M., Eds.; Oxford University Press: Oxford, 1986.

[14] Flory, P. J. *Principles of Polymer Chemistry*, 1st ed.; Cornell University Press: Ithica, NY, 1953.

[15] Fraaije, J. G. E. M. *The Journal of Chemical Physics* **1993**, *99*, 9202.

[16] Fraaije, J. G. E. M.; van Vlimmeren, B. A. C.; Maurits, N. M.; Postma, M.; Evers, O. A.; Hoffmann, C.; Altevogt, P.; Goldbeck-Wood, G. *The Journal of Chemical Physics* **1997**, *106*, 4260.

[17] Paradiso, S. P.; Delaney, K. T.; García-Cervera, C. J.; Ceniceros, H. D.; Fredrickson, G. H. *ACS Macro Letters* **2014**, *3*, 16–20.

[18] Kawasaki, K.; Sekimoto, K. *Macromolecules* **1989**, *22*, 3063–3075.

[19] de Gennes, P. G. *The Journal of Chemical Physics* **1980**, *72*, 4756.

[20] Fredrickson, G. H. *The Equilibrium Theory of Inhomogenous Polymers*; 2006.

[21] Matsen, M. W. *Journal of Physics: Condensed Matter* **2002**, *14*, R21–R47.

[22] Prosperetti, A.; Plesset, M. S. *Physics of Fluids* **1984**, *27*, 1590.

[23] Viollaz, P. E.; Suarez, C. *Journal of Polymer Science: Polymer Physics Edition* **1984**, *22*, 875–879.

[24] Wodo, O.; Ganapathysubramanian, B. *Computational Materials Science* **2012**, *55*, 113–126.

[25] Petschek, R. G.; Metiu, H. *The Journal of Chemical Physics* **1983**, *79*, 3443.

[26] van Vlimmeren, B.; Fraaije, J. *Computer Physics Communications* **1996**, *99*, 21–28.

[27] Badalassi, V.; Ceniceros, H.; Banerjee, S. *Journal of Computational Physics* **2003**, *190*, 371–397.

[28] Ceniceros, H. D.; Fredrickson, G. H. *Multiscale Modeling & Simulation* **2004**, *2*, 452–474.

[29] de Gennes, P. G. *Scaling Concepts in Polymer Physics*; Cornell University Press, 1979.

[30] Douglas, J.; Dupont, T. In *Numerical Solution of Partial Differential EquationsII*; HUBBARD, B., Ed.; Elsevier, 1971; pp 133–214.

[31] Frigo, M.; Johnson, S. *Proceedings of the IEEE* **2005**, *93*, 216–231.

[32] Joo, W.; Park, M. S.; Kim, J. K. *Langmuir* **2006**, *22*, 7960–3.

[33] Glass, R.; Moller, M.; Spatz, J. P. *Nanotechnology* **2003**, *14*, 1153–1160.

[34] Oss-Ronen, L.; Schmidt, J.; Abetz, V.; Radulescu, A.; Cohen, Y.; Talmon, Y. *Macromolecules* **2012**, *45*, 9631–9642.

[35] Huang, H.; Zhang, F.; Hu, Z.; Du, B.; He, T.; Lee, F. K.; Wang, Y.; Tsui, O. K. C. *Macromolecules* **2003**, *36*, 4084–4092.

[36] Brinker, C. J.; Lu, Y.; Sellinger, A.; Fan, H. *Advanced Materials* **1999**, *11*, 579–585.

[37] Jung, A.; Filiz, V.; Rangou, S.; Buhr, K.; Merten, P.; Hahn, J.; Clodt, J.; Abetz, C.; Abetz, V. *Macromolecular rapid communications* **2013**, *34*, 610–5.

[38] Albert, J. N. L.; Epps III, T. H. *Materials Today* **2010**, *13*, 24–33.

[39] Osuji, C. O. *Macromolecules* **2010**, *43*, 3132–3135.

[40] Tran-Ba, K.-H.; Finley, J. J.; Higgins, D. A.; Ito, T. *The Journal of Physical Chemistry Letters* **2012**, *3*, 1968–1973.

[41] Phillip, W. A.; Hillmyer, M. A.; Cussler, E. L. *Macromolecules* **2010**, *43*, 7763–7770.

[42] Bates, F. S.; Fredrickson, G. H. *Annual Review of Physical Chemistry* **1990**, *41*, 525–57.

[43] Fredrickson, G. H.; Bates, F. S. *Annual Review of Materials Science* **1996**, *26*, 501–550.

[44] Leibler, L. *Macromolecules* **1980**, *13*, 1602–1617.

[45] Fasolka, M. J.; Mayes, A. M. *Annual Review of Materials Research* **2001**, *31*, 323–355.

[46] Helfand, E.; Tagami, Y. *The Journal of Chemical Physics* **1972**, *56*, 3592–3601.

[47] Matsen, M. W.; Schick, M. *Physical Review Letters* **1994**, *72*, 2660–2663.

[48] Gennes, P. D. *Scaling concepts in polymer physics*; Cornell University Press: New York, 1979.

[49] Bates, F. S. *Macromolecules* **1987**, *20*, 2221–2225.

[50] Doerk, G. S.; Cheng, J. Y.; Singh, G.; Rettner, C. T.; Pitera, J. W.; Balakrishnan, S.; Arellano, N.; Sanders, D. P. *Nature Communications* **2014**, *5*, 5805.

[51] Jeong, S.-J.; Kim, J. Y.; Kim, B. H.; Moon, H.-S.; Kim, S. O. *Materials Today* **2013**, *16*, 468–476.

[52] Griffiths, R. A.; Williams, A.; Oakland, C.; Roberts, J.; Vijayaraghavan, A.; Thomson, T. *Journal of Physics D: Applied Physics* **2013**, *46*, 503001.

[53] Luo, M.; Epps, T. H. *Macromolecules* **2013**, *46*, 7567–7579.

[54] Bal, M.; Ursache, A.; Tuominen, M. T.; Goldbach, J. T.; Russell, T. P. *Applied Physics Letters* **2002**, *81*, 3479.

[55] Mokarian-Tabari, P.; Collins, T. W.; Holmes, J. D.; Morris, M. A. *ACS Nano* **2011**, *5*, 4617–4623.

[56] Baruth, A.; Seo, M.; Lin, C. H.; Walster, K.; Shankar, A.; Hillmyer, M. A.; Leighton, C. *ACS Applied Materials & Interfaces* **2014**, *6*, 13770–13781.

[57] Singh, G.; Batra, S.; Zhang, R.; Yuan, H.; Yager, K. G.; Cakmak, M.; Berry, B.; Karim, A. *ACS Nano* **2013**, *7*, 5291–5299.

[58] Park, S.; Lee, D. H.; Xu, J.; Kim, B.; Hong, S. W.; Jeong, U.; Xu, T.; Russell, T. P. *Science* **2009**, *323*, 1030–1033.

[59] Feng, X.; Tousley, M. E.; Cowan, M. G.; Wiesenauer, B. R.; Nejati, S.; Choo, Y.; Noble, R. D.; Elimelech, M.; Gin, D. L.; Osuji, C. O. *ACS Nano* **2014**, *8*, 11977–11986.

[60] Tang, C.; Wu, W.; Smilgies, D.-M.; Matyjaszewski, K.; Kowalewski, T. *Journal of the American Chemical Society* **2011**, *133*, 11802–11809.

[61] Hur, S.-M.; Khaira, G. S.; Ramírez-Hernández, A.; Müller, M.; Nealey, P. F.; de Pablo, J. J. *ACS Macro Letters* **2015**, *4*, 11–15.

[62] Crank, J. *The Mathematics of Diffusion*; Oxford University Press, 1975.

[63] Zettl, U.; Knoll, A.; Tsarkova, L. *Langmuir* **2010**, *26*, 6610–6617.

[64] Helfand, E. *The Journal of Chemical Physics* **1972**, *56*, 3592.

[65] Naughton, J. R.; Matsen, M. W. *Macromolecules* **2002**, *35*, 5688–5696.

[66] Fredrickson, G. H.; Leibler, L. *Macromolecules* **1989**, *22*, 1238–1250.

[67] Olvera de la Cruz, M. *The Journal of Chemical Physics* **1989**, *90*, 1995.

[68] Lodge, T. P.; Hanley, K. J.; Pudil, B.; Alahapperuma, V. *Macromolecules* **2003**, *36*, 816–822.

[69] de Gennes, P. G.; Prost, J. *The Physics of Liquid Crystals*; Oxford University Press, 1974.

[70] Gowd, E. B.; Böhme, M.; Stamm, M. *IOP Conference Series: Materials Science and Engineering* **2010**, *14*, 012015.

[71] Matsen, M. W. *Macromolecules* **2003**, *36*, 9647–9657.

[72] Fredrickson, G. *The Equilibrium Theory of Inhomogeneous Polymers*; Oxford University Press, 2006.

[73] Guo, Z.; Zhang, G.; Qiu, F.; Zhang, H.; Yang, Y.; Shi, A.-C. *Physical Review Letters* **2008**, *101*, 028301.

[74] Delaney, K. T.; Fredrickson, G. H. *Computer Physics Communications* **2013**, *184*, 2102–2110.

[75] Ginzburg, V. V.; Weinhold, J. D.; Trefonas, P. *Journal of Polymer Science Part B: Polymer Physics* **2015**, *53*, 90–95.

[76] Bates, F. S.; Schulz, M. F.; Khandpur, A. K.; Frster, S.; Rosedale, J. H.; Almdal, K.; Mortensen, K. *Faraday Discussions* **1994**, *98*, 7.

[77] Matsen, M. W. *The Journal of Chemical Physics* **2000**, *113*, 5539.

[78] Drolet, F.; Fredrickson, G. H. *Physical Review Letters* **1999**, *83*, 4317–4320.

[79] Tureau, M. S.; Rong, L.; Hsiao, B. S.; Epps, T. H. *Macromolecules* **2010**, *43*, 9039–9048.

[80] Man, W.; Florescu, M.; Williamson, E. P.; He, Y.; Hashemizad, S. R.; Leung, B. Y. C.; Liner, D. R.; Torquato, S.; Chaikin, P. M.; Steinhardt, P. J. *Proceedings of the National Academy of Sciences* **2013**, *110*, 15886–15891.

[81] Matsen, M. W.; Thompson, R. B. *The Journal of Chemical Physics* **1999**, *111*, 7139.

[82] Shi, A.-C.; Li, B. *Soft Matter* **2013**, *9*, 1398–1413.

[83] Matsen, M. W. *Macromolecules* **2012**, *45*, 2161–2165.

[84] Yi, H.; Bao, X.-Y.; Zhang, J.; Bencher, C.; Chang, L.-W.; Chen, X.; Tiberio, R.; Conway, J.; Dai, H.; Chen, Y.; Mitra, S.; Wong, H.-S. P. *Advanced Materials* **2012**, *24*, 3107–3114.

[85] Hannon, A. F.; Ding, Y.; Bai, W.; Ross, C. A.; Alexander-Katz, A. *Nano Letters* **2014**, *14*, 318–325.

[86] Hannon, A. F.; Gotrik, K. W.; Ross, C. A.; Alexander-Katz, A. *ACS Macro Letters* **2013**, *2*, 251–255.

[87] Khaira, G. S.; Qin, J.; Garner, G. P.; Xiong, S.; Wan, L.; Ruiz, R.; Jaeger, H. M.; Nealey, P. F.; de Pablo, J. J. *ACS Macro Letters* **2014**, *3*, 747–752.

[88] Bosse, A. W.; Sides, S. W.; Katsov, K.; García-Cervera, C. J.; Fredrickson, G. H. *Journal of Polymer Science Part B: Polymer Physics* **2006**, *44*, 2495–2511.

[89] Hur, S.-M.; Garcia-Cervera, C. J.; Kramer, E. J.; Fredrickson, G. H. *Macromolecules* **2009**, *42*, 5861–5872.

[90] Gaing, Z.-L. *IEEE Transactions on Energy Conversion* **2004**, *19*, 384–391.

[91] Nanvala, H. B.; Awari, G. K. *International Journal of Engineering and Technology* **2011**, *3*, 80–86.

[92] Bratton, D.; Kennedy, J. Defining a Standard for Particle Swarm Optimization. 2007 IEEE Swarm Intelligence Symposium. 2007; pp 120–127.

[93] Bonabeau, E.; Dorigo, M.; Theraulaz, G. *Swarm Intelligence: From Natural to Artificial Systems*, 1st ed.; Oxford University Press: New York, New York, 1999.

[94] Shi, Y.; Eberhart, R. A modified particle swarm optimizer. 1998 IEEE International Conference on Evolutionary Computation Proceedings. IEEE World Congress on Computational Intelligence (Cat. No.98TH8360). 1998; pp 69–73.

[95] Eberhart, R.; Kennedy, J. A new optimizer using particle swarm theory. MHS'95. Proceedings of the Sixth International Symposium on Micro Machine and Human Science. 1995; pp 39–43.

[96] Liang, J.; Qin, A.; Suganthan, P.; Baskar, S. *IEEE Transactions on Evolutionary Computation* **2006**, *10*, 281–295.

[97] Blackwell, T. B.; Bentley, P. *Proceedings of the Genetic and Evolutionary Computation Conference* **2002**, 19–26.

[98] Yi, H.; Latypov, A.; Wong, H.-S. P. Computational simulation of block copolymer directed self-assembly in small topographical guiding templates. Proceedings of SPIE. 2013; p 86801L.

[99] Stoykovich, M. P.; Kang, H.; Daoulas, K. C.; Liu, G.; Liu, C.-C.; de Pablo, J. J.; Müller, M.; Nealey, P. F. *ACS Nano* **2007**, *1*, 168–175.

[100] E, W.; Ren, W.; Vanden-Eijnden, E. *Physical Review B* **2002**, *66*, 052301.

[101] Takahashi, H.; Laachi, N.; Delaney, K. T.; Hur, S.-m.; Weinheimer, C. J.; Shykind, D.; Fredrickson, G. H. *Macromolecules* **2012**, *45*, 6253–6265.

[102] Qin, J.; Khaira, G. S.; Su, Y.; Garner, G. P.; Miskin, M.; Jaeger, H. M.; de Pablo, J. J. *Soft Matter* **2013**, *9*, 11467.

[103] Hansen, N.; Ostermeier, A. *Evolutionary Computation* **2001**, *9*, 159–195.

[104] Yuhui Shi,; Eberhart, R. Fuzzy adaptive particle swarm optimization. Proceedings of the 2001 Congress on Evolutionary Computation (IEEE Cat. No.01TH8546). 2001; pp 101–106.

[105] Mansky, P. *Science* **1997**, *275*, 1458–1460.

[106] Maldovan, M.; Urbas, a. M.; Yufa, N.; Carter, W. C.; Thomas, E. L. *Physical Review B* **2002**, *65*, 165123.

[107] Saranathan, V.; Osuji, C. O.; Mochrie, S. G. J.; Noh, H.; Narayanan, S.; Sandy, A.; Dufresne, E. R.; Prum, R. O. *Proceedings of the National Academy of Sciences* **2010**, *107*, 11676–11681.